Magnetotelluric Investigations of the Kīlauea Volcano, Hawaii

G. M. Hoversten [1]

Erika Gasperikova [1]

Randall Mackie [2]

David Myer [3]

Jim Kauahikaua [4]

Greg. A. Newman [1,5]

Nestor Cuevas [6]

[1] Lawrence Berkeley National Laboratory

[2] CGG Multiphysics

[3] BlueGreen Geophysics LLC

[4] United States Geologic Survey

[5] Sandia National Laboratory

[6] Schlumberger

This article has been accepted for publication and undergone full peer review but has not been through the copyediting, typesetting, pagination and proofreading process, which may lead to differences between this version and the Version of Record. Please cite this article as doi: 10.1029/2022JB024418.

KEY POINTS

- Inverted 3D resistivity has high spatial correlation with seismic Vp/Vs from Dawson et al. (1999).
- Melt fractions of 0.096 and 0.117 are predicted for magma bodies beneath Kīlauea and Puʻuʻōʻō respectively.
- The Kīlauea summit magma chamber is well imaged between 0 and -2 km elevations by 3D resistivity.

ABSTRACT

In 2002 and 2003 a collaborative effort was undertaken between Lawrence Berkeley National Laboratory, Sandia National Laboratories, the USGS Menlo Park, the USGS Hawaiian Volcano Observatory, and Electromagnetic Instruments Inc. to study the Kīlauea volcano in Hawaii using the magnetotelluric (MT) technique. The work was motivated by a desire to improve understanding of the magma reservoirs and conduits within Kīlauea and the East and Southwest Rift zones, which has implications for understanding Kīlauea's plumbing system. An improved understanding of the rift zones has implications in understanding large-scale landslides that are generated in the Hilina Slump, which produce significant impacts on coastal communities. Up to eight stations operated simultaneously, with multiple remote reference sites, and data were processed using multi-station robust processing techniques. In total, data were acquired at 70 sites over the Southwest and East rift zones. Good to excellent quality data were obtained even in the harshest conditions, such as those encountered on the fresh lava flows of the East Rift Zone (ERZ),

where electrical contact resistances are on the order of 100 kΩ. A three-dimensional (3D) MT model study was done to guide interpretation of the observed MT measurements. Synthetic modeling demonstrates that conductive bodies in the upper 3 km can be spatially resolved where MT station sampling is good. Resistivity anomalies in the 3D inversions have a high degree of spatial correlation with previously published seismic velocity anomalies beneath Kīlauea. Melt fractions between 0.096 and 0.117 are calculated for the Kīlauea and Puʻuʻōʻō low resistivity anomalies, respectively.

PLANE LANGUAGE SUMMARY

Magnetotelluric (MT) data collected on the Island of Hawaiʻi on Kīlauea volcano and its associated rift zones in 2002 and 2003 have been inverted to produce a three-dimensional resistivity model. The resistivity model is compared to published models of seismic velocity and Vp/Vs ratio derived from earthquake data acquired by the Hawaiian Volcano Observatory. In areas where the velocity models have good data coverage and high sensitivity, such as over the summit magma chamber, the MT derived resistivity, and the seismic derived Vp and Vp/Vs models have a very high degree of spatial correlation. The high correlation between independent models increases the confidence in both models. Melt fractions of 0.096 and 0.117 are calculated from the inverted resistivities for low resistivity anomalies beneath Kīlauea and Puʻuʻōʻō respectively. This work demonstrates that high-quality MT data can be acquired in the difficult field conditions present on an active volcano and points the way forward for future improved acquisitions.

1.0 INTRODUCTION

Historically, the Island of Hawai‘i is one of the most seismically active areas in the world. Over the period of human recording, several large-magnitude earthquakes, such as the *M 7.9* Ka‘ū earthquake in 1868 (Lipman *et al.,* 1985), the *M 7.7* Kalapana earthquake in 1975 (Nettles and Ekström, 2004), and the *M 6.9* event in 2018 (Lay et al., 2018) have occurred. Additionally, there is a nearly constant sequence of smaller earthquakes. Earthquakes in and around Kīlauea volcano have been recorded by the Hawaiian Volcano Observatory (HVO) since 1912. The abundance of earthquake data has led to considerable study of the seismic velocity structure of Kīlauea (e.g., Ryan, 1987, 1988; Okubo et al., 1997; Dawson et al., 1999; Haslinger et al., 2001; Lin et al., 2014a, 2014b to cite but a few). An improved understanding of the magma reservoirs and conduits within Kīlauea, the East rift zone (ERZ) and Southwest rift zone (SWRZ) has major academic as well as practical implications since major eruptions cause significant disruptions to the local inhabitants as well as large-scale property damage. Additionally, large-scale landslides generated in the Hilina Slump, an area on the southeast flank of Kīlauea that extends from the East Rift Zone to the edge of deep water, can cause destructive tsunamis that impact widespread coastal communities (e.g., Lipman et al. (1985); Tilling et al. (1976); Day et al. (1999); Ward (2002); Morgan and Clague (2003).

Understanding the 3D electrical resistivity structure of active Hawaiian volcanoes is a natural complement to those aspects of the internal structure inferable from magma-induced deformation and related rock fractures. Magma-induced pressure perturbations are reflected in micro-seismicity distributions (Klein et al., 1987), seismic *b*-value distributions (Wyss et al., 2001;

Chouet et al., 2010), traditional leveling-based deformation (Dvorak and Dzurisin, 1997; Delaney et al., 1993), tilt studies (e.g., Dvorak and Okamura, 1987; Poland et al., 2014), Global Positioning System (GPS)-based shield and crustal extension studies (Owen et al., 1995, Cervelli and Miklius, 2003; Miklius et al., 2005; Poland et al., 2012; Wright and Klein, 2014), synthetic aperture radar interferometric work (Zebeker et al., 2000; Massonnet and Sigmundsson, 2000, Lundgren et al., 2013) or studies derived by merging deformation, geologic, and micro-seismic surveys with the mechanical modeling of internal pressure centers and high-temperature, high-pressure rock properties (Ryan et al., 1981; Ryan, 1987, 1988; Daniels et al., 2012). All such studies are tied, variously, to the spatial distribution of magma pressure sources. Hence, all the above investigations indirectly relate to melt distribution but geophysical methods such as seismic, gravity, and electrical resistivity directly image these regions.

Early electrical and electromagnetic (EM) surveys of Kīlauea used controlled sources of energy to measure the EM response of the subsurface (Kauahikaua, 1982; Jackson, et al., 1985; 1986; Bartel and Jacobson, 1987). These experiments resulted in limited depth penetration due to modest transmitter power. In contrast, the MT method uses naturally generated EM fields as a source, eliminating the reliance on a transmitter, generally increasing the depth of investigation, and simplifying logistics in the field. MT has been used for remote detection and imaging of volumes of partially molten magma beneath volcanic systems for many years (e.g., Park and Torres-Verdin, 1988; Mogi and Nakamura, 1993; Hill et al., 2009; Wannamaker et al., 2009; Ingham et al., 2009; Ogawa et al., 2014; Aizawa et al., 2014; Comeau et al., 2016; Zhang et al., 2016; Ye et al., 2018; Tseng et al., 2020; Matsunaga et al., 2020a, 2020b; Yang et al. 2021).

The survey was conducted using remote reference sites in combination with robust data processing techniques, as has been done at other volcanic centers (e.g., Nolasco et al., 1998; Ogawa et al., 1999; Bayrak et al., 2000). The work described here was a collaborative effort between Lawrence Berkeley National Laboratory, Sandia National Laboratories, Electromagnetic Instruments Inc. (later acquired by Schlumberger), and the Hawaiian Volcano Observatory of the U.S. Geological Survey. Initial findings were presented by Hoversten (2003), but circumstances delayed further work for nearly 20 years. The time lag between data acquisition and writing of this paper had the unintended benefit that 3D MT inversion has significantly advanced, making the interpretation of this data set by a full 3D inversion of the measured impedance tensor elements relatively easy on modest cluster resources. We have undertaken a 3D MT study of Kīlauea Volcano, with the first phase of data acquisition completed in August 2002 and the second phase completed in June 2003. A total of 70 MT sites were acquired. To our knowledge, this was the first successful published MT data acquisition and interpretation on Kīlauea. Because the data acquisition and interpretation reported here is twenty years old and occurred before the major eruptive sequence of 2018 it serves to document the pre-2018 setting and can be used to look for changes beneath Kīlauea caused by the latest eruptive sequence. Hence, this work serves as a baseline for imaging any changes caused by the 2018 and later eruption sequences.

We begin with a description of the field experiment strategy. A summary of the data acquisition approach and the results of the survey with comments on data quality and integrity are presented in Supplement 1. Next, we conduct a 3D numerical modeling experiment to demonstrate model resolution, given our data coverage. This is followed by 3D inversion of the data and comparison to contemporary seismic model and earthquake hypocenter results. Finally, volume averaged conductivity of conductive anomalies beneath Kīlauea and Puʻuʻōʻō are used to predict melt fractions.

We describe all depths in terms of elevation relative to sea level. Thus, an elevation of -1 km is 1 km below sea level.

2.0 EXPERIMENT DESIGN

The overall experiment design reflects our objective of characterizing Kīlauea's internal electrical structure in 3-D. Recognizing that the active magmatic system is comprised of a central magma ascent core region deep beneath the summit caldera (Ryan, 1988, Poland et al. 2014) and with two radiating rift zones**,** we have organized the arrays of MT acquisition sites into three groups that promote dissecting the geometry of the system at depth. These are *caldera-crossing*, *rift-zone-crossing*, and *rift zone-parallel* arrays. Site locations have arbitrary but unique labels, starting with *"S"*, *"J"*, and *"H"*, respectively. Figure 1 illustrates the MT site locations along with major roads, calderas, and major lava flows contemporaneous with the MT survey. The geometry of the site locations is not uniform or ideal due to access and budget limitations. However, the site sampling is adequate to demonstrate the potential of MT for imaging. Plate 1 of Ryan (1988) illustrates the 3D internal structure of Kīlauea with respect to surface geomorphic features and the subsurface regions sampled by the MT measurement sites. The outline of the rift zones at -1 km elevation, from Ryan (1988), is overlaid on Figure 1 and is used in building the synthetic resistivity models to be described later.

The southwestern portion of the summit/caldera complex hosts an MT site above the 1,262 m deep NSF-funded research drill hole (Keller et al., 1979). This has been identified as the "Keller-NSF" site in the text, and is simply denoted as "Keller", in Figure 1. The Keller-NSF site provides the best constraint on the 3D model for comparison to the Keller-NSF resistivity log. In addition, a quiet, remote reference site has been an integral component of the overall experiment design. The geomorphic "saddle" formed between the masses of Mauna Loa and Mauna Kea has provided a relatively noise-free location, removed from the incidental electrical noise contamination associated with well-traveled highways and small communities. This site is near the geometric center of the island and is simply referred to as the Saddle within the text.

3.0 ACQUISITION

The initial phase of data acquisition, conducted during August 2002, consisted of acquiring MT data in the vicinity of Kīlauea caldera, as well as within the ERZ and the SWRZ (Figure 1). The survey was designed to make use of multiple remote reference sites and multi-station robust processing techniques (Egbert 1997), with as many as eight acquisition systems operating simultaneously. Excellent quality data were obtained, even in harsh and highly resistive environments, such as the fresh lava flows of the ERZ, where electrical contact resistances were extremely high. Copper Copper-Sulfate electrodes were used throughout the survey. Where possible, holes were dug into the soil and filled with a mixture of bentonite clay and water, and the electrodes placed in the clay. On the fresh lava flows, low pockets in the lava were filled with the clay-water mixture as a bed for the electrodes. All clay was removed from each electrode site after data recording. The lowest contact resistance measured was 3–5 kΩ (sites S03 and S04). Average contact resistance of 20–60 kΩ was measured at sites well off the fresh lava flows (e.g., sites S24, H01, and H02), and values in the range 80–90 kΩ were measured on the lava flows themselves (sites J07, J16, and J18).

The logistics of MT experiments over wide sectors of Kīlauea are challenging in several ways. These challenges include sparse road access, the policies of operation within the Hawai‘i Volcanoes National Park, and operating on terrain that varies from tropical rainforest to desert. Only horizontal magnetic field sensors were deployed. MT sites requiring helicopter access were recorded using only electric (E) fields to reduce weight and setup time. This approach was followed by Cagniard (1953) where the difficulty, at the time, of placing magnetometer on the sea floor caused them to measure magnetics onshore and electric fields offshore. One of the helicopter access sites had data processed with and without local magnetic (H) data; the processing is described in Supplement 1, where the comparison (Figure S1-S10) demonstrates the validity of using remote H fields with local E fields for impedance calculations. During the 2002 acquisition (35 sites), data were preliminarily processed in the field at each site before the site was removed. This insured that hardware or environmental problems could be addressed with minimal data loss. The downside was increased time/cost per site. In 2003, due to a dwindling budget, processing was not done at sites prior to moving them. This resulted in reduced frequency bands of good data at the 2003 sites compared to 2002.

MT data were recorded in three frequency bands, with sampling frequencies of 500 Hz, 50 Hz, and 6.25 Hz, respectively. The low-frequency data were then decimated down to 0.001 Hz. The 50 Hz data covered a frequency range from 0.01 to 10 Hz, and the 500 Hz data covered a frequency range from 0.1 Hz to 125 Hz. Low-frequency data were acquired up to three days. Both the 500 Hz and the 50 Hz bands (30 minutes) were recorded every four hours to increase the probability of acquiring data during times of high signal-to-noise ratios. Each frequency band was processed independently, and then the highest quality data with the best signal-to-noise ratios were combined to produce the final output impedance curve. For a given local MT site, many channels of remote E and H data were available for use in the final signal processing (Egbert 1997). Local channels (E and H time series data) were the same for low and high-frequency bands. The remote channels could be different for times when we took down completed sites and powered up new ones. We were not able to start and stop all the sites at the same time. We took advantage of all channels running at any time. Therefore, for a given site, the final impedance curves over the entire frequency range may be derived from differing channels from differing sites used as remote references within the various frequency bands. This is important to remember, since different remote channels may have been used for the high and low frequency bands.

4.0 THE RELATIONSHIP BETWEEN ROCK PROPERTIES AND GEOPHYSICAL PARAMETERS

To interpret the electrical resistivity images produced by inversion of the MT data in terms of geology requires an understanding of the factors that govern a rock's electrical resistivity. The most important properties that control the bulk electrical resistivity of the rocks on Kīlauea are the rock type, fluid saturation, porosity, temperature, and the salinity of the pore water.

Kīlauea is composed mostly of tholeiitic basalt that occurs as thin, sub-horizontal lava flows. Kīlauea is composed of layer upon layer of such flows from the seafloor to the present surface (Kauahikaua et al., 1986). Because these lava flows have high permeability, they can be considered either fully saturated (below the water table) or only partially wetted above the water table. Previous surface and borehole studies (Zohdy and Jackson, 1969; Zablocki et al., 1974) have shown the saturation to be a sharp transition at the water table.

The effect of porosity, pore water salinity, and temperature on the bulk resistivity of tholeiitic basalt is summarized in Figure 2 (Kauahikaua et al., 1986, Figure 20 of that report). For low temperatures (below 600 ^{o}C) two cases are considered: 1) low salinity pore water (ground water from the summit research hole (Kauahikaua, 1982) with water resistivity (ρ_w) of 2 Ωm and salinity (S) of 3 parts per thousand and 2) sea water with ρ_w of 0.21 Ωm and S of 35 ppt. Below 600 ^{o}C conduction is through the pore fluids, above 600 ^{o}C conduction through the rock matrix exceeds conduction through the pore electrolyte and the resistivity decreases with increasing temperature. At 1200 ^{o}C the dry magma resistivity from Figure 2 is 0.55 Ωm, for comparison, the SIGMELTS online tool (Pommier and Le-Trong, 2011) for 0.001 water %wt (the lowest value the tool calculates resistivity for) produces 0.37 Ωm.

The seismic velocity of rock is also a function of porosity and fluid saturation, although less strongly so than is electrical resistivity. Both fracturing and melting decrease seismic velocity. No experimental data on the velocity of partial molten rock under those conditions found at Kīlauea are available. However, theoretical calculations (Mavko, 1980; Takei, 1998) show that a 1% melt fraction in a mafic rock decreases the velocity by 1% and that 10% melt can cause V_p to decrease on the order of 10% while V_s will decrease on the order of 20%. This would mean that partial melt zones should have lowered V_p and elevated V_p/V_s ratio compared to non-molten rock. Fracture zones within the basalt flows should also exhibit lower V_p due to increased porosity and reduced frame bulk modulus but should not show the anomalous V_p/V_s ratio of partial melt zones.

A few inferences of the resistivity of Kīlauea magma have been made via electromagnetic measurements. Smith et al. (1988), Smith and Frischknect (1980) inferred a resistivity of 2.07 Ωm at 1070 ^{o}C for molten magma in the Kīlauea Ike crater after the 1962 eruption. Thirteen years later after some cooling Hermance and Colp (1982) estimated a resistivity of 2.3 Ωm for the same magma body. From Figure 2 pure melt zones beneath Kīlauea in the 1000 to 1200 ^{o}C range should have electrical resistivity between 0.5 and 2.5 Ωm. Depending on the depth and temperature of the melt and the MT frequencies that penetrate those regions, there will be spatial averaging in partial melt between melt and crystal, resulting in MT seeing higher resistivities than pure melt. Highly fractured fault zones should also exhibit lower velocity and resistivity due to fracturing and increased water content. Far from the coast, we would expect the saturation fluids to be fresh water, while close to the coast and at elevations below sea level fracture systems may be saturated with more saline sea water that would result in more conductive fracture zones compared to fracture zones away from the coast.

5.0 3D INVERSION OF MT DATA

The proprietary inversion software used here is a nonlinear conjugate gradient algorithm. Details can be found in Hoversten et al. (2021), Mackie et al. (2020), Rodi and Mackie (2001) and in Supplement 2.

In this work we carried out inversions of MT data where the forward modeling function numerically solves the Maxwell equations in three dimensions using the Finite Integration Technique (FIT) *(e.g., Weiland, 1977; Clemens and Weiland, 2001). The FIT is a discrete, but exact, reformulation of the Maxwell equations in their integral form that provides a generalized scheme for solving EM problems in discrete space and admits arbitrary geometries and coordinate systems. FIT represents the only known theory that maintains the analytical properties of EM fields going from real space to discrete space (Weiland, 1996). Applying FIT on orthogonal cartesian grids leads to the standard Yee staggered grids (Yee, 1966), but the technique is easily extended to non-orthogonal grids. More details on the implementation can be found in Mackie and Watts (2012).*

6.0 SYNTHETIC MODEL

To understand the spatial resolution of the 3D inverse models of the MT data collected on Kīlauea, a synthetic model was constructed based on a simplified conceptualization of the magma conduit from the mantle to the surface and the rift zones. The background resistivity is 100 Ωm. The model encompasses the entire Island of Hawai‘i with the surrounding ocean up to 80 km to the east and south (near the modeled MT sites) with a minimum of 30 km of ocean to the north, although at different resolutions. The geometry of the rift zones is taken from Ryan (1988) for the elevation interval -1 to -2 km. The rift zones are given a resistivity of 1 Ωm, which would represent a high degree of interconnected basaltic melt as shown in Figure 2. The top and bottom of the conductive rift zones are horizons that run parallel to the surface elevation but shifted down by 0.8 and 2.8 km respectively. The conduit is represented as a nearly circular vertical column extending from the base of the conductive rift zones to elevation -14.7 km. The elevation of -14.7 km is taken as the transition between oceanic crust and the Moho beneath our survey area (Li et al., 1992). The north-south extent is 6 km, and the east-west extent is 5 km. The conduit geometry is loosely based on Figure 1 from Ryan (1988). The conduit is assigned a resistivity of 1000 Ωm which corresponds to high velocity solidified gabbro-ultramafic cumulates (Okubo et al., 1997). The column is centered just south of the surface expression of the caldera, based on visual inspection of the Ryan (1988) model figures. In addition to the simplified Kīlauea plumbing, two additional zones of anomalous low resistivity are included in the model. One represents a hypothetical fluid filled fracture zone in the Hilina fault system that lies south of the Kīlauea caldera. This zone is assigned a resistivity of 10 Ωm at an elevation between 0.2 and -2 km. The second zone represents a possible deep magma chamber as hypothisized by Lin et al. (2014b). This zone is given a resistivity of 1 Ωm at an elevation between -7.5 and -10.5 km. The model is summarized in Figure 3, where elevation slices at -1 and -9 km are shown in Figure 3a and Figure 3b, respectively. A traverse through the center of the rift zones is shown in Figure 3c and a southwest to northeast traverse is shown in Figure 3d.

Four synthetic data sets were generated using the frequencies and site locations of the acquired field data. The models are: 1) the model shown in Figure 3 with all four anomolous resistivity zones and the acquired frequencies at each site, referred to as Model 1, 2) same as Model 1 but without the resistive conduit, referred to as Model 2, 3) same as Model 1 but without the hypothesized deep magma zone, refered to as Model 3, 4) same as Model 1 using site locations from the field data but with all frequencies (35 frequencies spanning 0.001 to 100 Hz) at all sites, referred to as Model 4. The total number of complex impedance data for Models 1 through 3 are 7,096, whereas Model 4, with all frequencies at all sites, has 19,040 complex impedance data. Comparison of Models 1 and 2 tests the sensitivity, or lack thereof, to the conductive rift zones and the resistive conduit in the field data. Comparison of Models 1 and 3 tests the sensitivity to the potential deep magma zone. Comparison of Models 1 and 4 tests the effects of limited frequency coverage at some sites compared to an ideal collection of all frequencies at all sites.

Since only horizontal E and H fields were measured in the field, only four components of the impedance tensor (Z) are used. These are Z_{xx}, Z_{xy}, Z_{yx} and Z_{yy} with x oriented east-west and y north-south. The synthetic data were computed on a finer mesh than is used for the inversions. The forward mesh contained 7,188,496 cells, whereas the inversion mesh contained only 4,106,888 cells. The difference in forward and inverse meshes introduces different numerical noise into each calculation, thus attempting to make the inverse problem a little more realistic and not commit what is referred to in the inversion community as the "inverse crime" (Wirgin, 2004). Modeling MT data on islands does not require any special treatment of the ocean other than its inclusion in the 3D model, with appropriate resistivity values, out to sufficiently large distances so that the model boundaries are accurately represented. The MT modeling code used in this work is a proprietary commercial code that has a long history of use and has been benchmarked against semi-analytical results and other numerical codes (e.g., Miensopust et al., 2013; Mackie and Watts, 2012). It has been used extensively for commercial exploration projects including oil and gas, geothermal, mining, and marine EM (e.g., Hoversten et al., 2021; Mackie et al., 2020; Soyer et al., 2018).

The synthetic model data were contaminated with Gaussian noise. The noise added to the real and quadrature components of Z_{xx} and Z_{xy} is a zero-mean Gaussian with standard deviation of 10% of the magnitude of the mean of (Z_{xx} + Z_{xy}). Similarly, the noise added to the real and quadrature components of Z_{yx} and Z_{yy} is a zero-mean Gaussian with standard deviation of 10% of the magnitude of mean of (Z_{yx} + Z_{yy}). The starting model for the 3D inversions is a 100 Ωm half-space beneath the topography of the Island of Hawai‘i, with the ocean included a priori. The 3D finite difference meshes used for inversion of the synthetic and field data sets are identical.

6.1 Model with site geometry and frequencies from field acquisition

Figure 4 compares the synthetic Model 1 (Figure 4a) and the inversion of the synthetic model data (Figure 4b) for the -1 km elevation slice. The area shown encompasses 68 of the 70 sites recorded. Two remote reference sites on and just to the south of the saddle between Mauna Loa and Mauna Kea are not used in the inversion, as is the case for the field data. Exclusion of the two remote sites greatly reduces the size of the computation meshes and hence the computer run times. Depth sections along the rift zones traverse and the southwest to northeast traverse are shown in Figure 5.

The approximate resolution (R) was calculated to give a qualitative definition between well-resolved and poorly-resolved parts of the inverse model. The approximate R (Backus and Gilbert, 1968; Jackson, 1972) is given by $A^T V^{-1} A$ where A is an approximation to the partial derivative matrix (Jacobian), and V is the inverse of the data covariance matrix, which is assumed diagonal. The approximation comes from using 1D adjoint fields (and the true 3D forward fields) instead of 3D adjoint fields (Farquharson and Oldenburg, 1996). Other practitioners such as Lin et al. (2014a), have used an R value of 0.3 to define the demarcation between well and poorly resolved. However, in this synthetic example, some features of the model are correctly located where R values between 0.2 and 0.3 exist. For example, between 25 – 35 km in Figure 5c, the model is poorly resolved even though R values are greater than 0.3. In addition, R values greater than 0.3 extend laterally away from site coverage where model reconstruction is poor. We conclude that the approximate resolution calculation resulting from the gradient algorithm cannot be used quantitatively but still contains qualitative information. That is, while a single value cannot be used to define a cut-off between good and poor resolution through the entire model, in general, areas of high-resolution values are correlated with well-resolved parts of the model while areas of low-resolution values are correlated with poorly resolved parts of the model. The transition between well- and poorly-resolved lies somewhere between 0.2 and 0.4.

We choose to define a confidence volume where we augment the calculated R with a masking polygon surrounding the MT sites whose edge is at least 2 km outside of the MT sites. The choice of 2 km as the distance is based on prior experience and the synthetic modeling shown here. The polygon is shown on Figure 4b as the dashed black line. The volume where the R values are greater than 0.3 inside of the mask polygon defines our confidence volume. Outside of this confidence volume model cells are shaded in all subsequent plots.

Two depth-sections through Model 1 are shown in Figure 5. MT sites that lie within a perpendicular distance of 2 km of the cross-sections are plotted as green inverse triangles on the depth-sections. Figure 5a shows the model depth-section along a traverse that runs down the center of the conductive rift zone, with the corresponding section through the inversion shown in Figure 5c. Figure 5b shows the southwest to northeast depth-section through Kīlauea and the Hilina fracture zone, with the corresponding section through the inversion shown in Figure 5d. Both depth-section traverses are marked on Figure 4a and 4b. Each inversion section has contours of R < 0.7 plotted. Higher R values concentrate near the surface and clutter the display.

Figures 4 and 5 show that in areas with high MT station density, the inversion recovers the spatial extent of the low resistivity rift zone quite accurately. The lateral resolution of the rift zone around the Kīlauea caldera and to the east of Puʻuʻōʻō where there are closely spaced MT sites is quite good. While the rift zones are spatially well resolved where there is site coverage, where there are gaps in site sampling along the rift zones, resolution is poor (e.g., around traverse bend points 4 and 5). The 10 Ωm body representing a fluid-filled fracture zone in the Hilina fault zone is resolved as a zone that is more conductive than the background but not as conductive as the rift zones. The plan view resolution (Figure 4b) is generally good, but definition is worse to the south away from the southern most MT sites. As is shown in the next section some of the loss of resolution of the rift zone and the deeper magma body is due at least in part to limited frequency content at many of the sites between traverse bends 3 and 5. Gaps in site coverage along this section also contribute to the loss of resolution.

In the rift zones near the caldera where the spatial distribution of low-resistivity closely matches the distribution in the true model, the low resistivity is concentrated in a smoothed region that is both smaller and has a lower minimum resistivity than the distribution in the true model (see distance 15 to 20 km Figure 5c). This is a common occurrence in spatially smoothed inversions where the filtering effect of the spatial smoothing acts to produce a Gibbs (Gibbs 1898) oscillation in the properties: the inverted resistivity overshoots high resistivity and undershoots low resistivities. Examples of this smoothing oscillation can be seen in Smith and Booker (1988), and Constable and Weiss (2006).

To derive a correction factor between inverted and in situ resistivity, it is useful to look at a volume average on the scale of the structures we are interested in. The volumes for averaging are defined by polygons in Easting and Northing and surfaces in elevation. For Kīlauea and Puʻuʻōʻō the polygons are the model polygon for the rift zones that are truncated in Easting based on where there is MT site coverage, and the surfaces are the model surfaces. These polygons are shown in black on Figure 4a. For the Hilina fault zone, the polygon and surfaces are from the model. The inverted conductivity within the volumes defined by the polygons and surfaces was averaged (Bigalke, 2000) and converted back to resistivity. The averaged conductivities converted to resistivity will from here on be referred to as “average resistivity”. The averaged resistivities for the low resistivity zones at Kīlauea, Puʻuʻōʻō, and Hilina fault system are 1.91 Ωm, 2.22 Ωm, and 19 Ωm respectively. The corresponding correction factors are 0.52, 0.45, and 0.52 respectively. These correction factors will be used later when we attempt melt fraction calculations based on the inverted resistivity from the field data at Kīlauea and Puʻuʻōʻō.

The inverse model shows a resistive feature extending to a depth that roughly corresponds to the resistive conduit to the mantle. This feature has an extension to depth where the resolution values are greater than 0.3. We will wait for comparison to the inverse model without the resistive conduit before reaching any conclusions about the ability of the inversion to resolve this resistive feature.

6.2 Synthetic model data fits

The inversion of Model 1 data shown in Figures 4 and 5 started with an overall RMS data misfit of 18.3 and converged to RMS 1.17 after 63 iterations. Figure 6 shows the RMS misfit break down by period in Figure 6a and by site in Figure 6b. Figure 6 also shows the number of samples for each calculated RMS value. In Figure 6a there are two groups of samples representing the 2002 (large number of samples) and 2003 (small number of samples). The smaller amount of data from

2003 are a result of the limited frequency bands at those sites. Figure 6b shows that the RMS misfit is fairly uniform from site to site across a range of number of samples and a range of acquisition conditions from tree covered forest lands (site S04) to pure lava flows (site J30). Figure 7 shows observed and calculated real and imaginary impedance curves for four sites sorted from west (S04) to east (J30). In general, the on-diagonal impedance elements, Z_{xx} and Z_{yy} are an order of magnitude smaller with larger errors than the off-diagonal elements, Z_{xy} and Z_{yx}. The fits to the larger Z_{xy} and Z_{yx} are better and contribute more to determination of the model.

6.3 Resolution of resistive conduit to the mantle

The results for the synthetic model without the resistive conduit to the mantle (Model 2) are shown in Figure 8c and Figure 8d. The inversion results for Model 1 are shown in Figure 8a and Figure 8b (replotted from Figure 4c and Figure 4d for comparison). The effects of the resistive conduit are subtle but visible. The inverse model with the conduit has higher resistivities in the conduit location that extend to greater depth than the inverse model without the conduit. Interestingly, the volume enclosed by an R value of 0.4 is slightly larger for the model with the resistive conduit. While there are noticeable differences in the inverse models with and without the resistive conduit the differences are so subtle that making an interpretation on them in field data would be challenging and subject to significant error in our opinion. If a resistive conduit to the mantle were to be resolvable, it would have to have larger spatial dimensions than used in the synthetic model. We will come back to this when the inversions of the field data are examined.

6.4 Effects of full frequency content

Finally, the effects of data with limited frequency content compared to having data at all frequencies at all sites (Model 4) are illustrated in Figure 9. Figure 9a and 9b show the inversion results with field acquisition defined frequencies at each site (same as Figure 8a and 8b). Figure 9c and 9d show the corresponding traverses when all frequencies are present at all sites. The positive impact of having all frequencies at all sites is most obvious on the rift zones traverse (Figure 9c), where the conductive rift between 20 and 35 km distance is significantly improved by the added frequency content. Of the ten sites near the traverse between bend 3 and 5 (20 to 35 km distance) only one (J30) has a nearly full frequency band (0.055 - 560 s). Of the other nine the shortest period is 7 s at one site with the remaining eight having only 10 s as the shortest periods. At 10 s, the skin depth in the 100 Ωm overburden is 15,900 m; in the 1 Ωm rift zone, the skin depth is 1590 m. Higher frequencies (shorter periods) in this section of the model make a considerable improvement in the inversion model resolution and should be a priority in any future acquisition. It should be noted that this area had exposed lava flows, where making electrical contact was difficult and wind noise in magnetometers laid on the lava (even with sandbags on top) was high.

The impact of the increased frequency range at all sites on the resolution of the resistive conduit to the mantle is minimal. The difference in resistivity models is not visually apparent on either traverse near the resistive conduit. Compare Figure 9a and Figure 9c, and Figure 9b and Figure 9d. The lack of significant improvement in resolution of the conduit beneath Kīlauea caldera is most likely due to the already good frequency coverage of most of the sites in this area.

6.5 Resolution of deep magma chamber

The shape and location of the proposed magma chamber in our synthetic Model 1 is derived from the Vp/Vs anomaly shown in Lin et al. (2014b) Figure 1B panel F. Two variants of Model 1 were run; one with the proposed magma chamber at 1 Ωm and one with the proposed magma chamber at 3 Ωm. Considering the six MT sites closest to the proposed magma chamber (p32, p20329, p24, j30, p17, p19), using the field acquisition frequencies, the change in the apparent resistivity and phase of the XY and YX modes as measured by the RMS was 0.27 when the body was 3 Ωm and 0.34 when it was 1 Ωm. These changes are within the assigned MT errors but are consistent in that the apparent resistivity curves go to lower values as the hypothetical body becomes less resistive, with the largest changes in the 10 to 1000 s band. For the data set with the acquisition frequencies, it is not obvious that a conductor is present by visual inspection of the inversion with the body (Figure 8a).

Comparing Figure 8a with Figure 8c shows that removing the resistive conduit enhances the effects of the deep magma body to the east. The effect is subtle, but the resistivity at bend 4 at elevation -9 km is 89 Ωm with the conduit and 74 Ωm without it, or a 17% decrease. The resistive conduit acts to divert electric currents that flow in the east-west plane around the conduit; removing it allows more current to flow into the deep conductor, thus increasing the response from the body. While the presence or absence of the resistive conduit can affect the response of the proposed deep magma chamber, the primary factor limiting resolution of the deep magma chamber is the overlying conductor that lies between elevations 0 and –2 km with an approximate conductance of 2000 S. Given the limited sensitivity to the deep magma body shown here, without other information interpreting these subtle changes in inverted resistivity would be problematic.

Comparing Figure 9a and Figure 9c demonstrates that having all frequencies at all sites between traverse bends 3 and 5 when the resistive conduit is present has also resulted in reduced resistivity in the volume around the deep magma body (between 23 and 33 km on the rift zone traverse). This implies that any future attempts to resolve deep magma bodies in the -8 to -12 km elevation range would benefit from high frequencies that better define the near-surface, allowing improved resolution at depth as well.

7.0 INVERSION OF FIELD DATA

The synthetic modeling not only served to probe model resolution but also to design a near optimal mesh that produced accurate results while running in the memory and run time constraints set by our compute resources. The mesh used in the synthetic model experiments was also used for the field data inversions. In this section we show resistivity models from the MT data inversion and compare them to borehole resistivity near the Kīlauea caldera and seismic models derived by Dawson et al. (1999) and Lin et al. (2014a). Additionally, we overlay the resistivity models with earthquake hypocenters generated by reprocessing HVO earthquake data by Lin et al. (2014a). Finally, in Supplement 2, we use a cross-gradient constraint to find a resistivity model that has gradients as close as possible to the Vp/Vs model from Lin et al. (2014a) in the -6 to -9 km elevation range where the Lin et al. (2014a) model has maximum resolution and compare this with the resistivity model from the MT data only.

7.1 Comparison to logged resistivity

The only borehole with an induction resistivity log in our area of interest is the National Science Foundation (NSF) well, located at the southern edge of the Kīlauea caldera (Keller et al., 1979). The Keller MT site, see Figure 1, is located within 100 m of the well location. The black curve in Figure 10 is the resistivity from the deep induction log (6FF4D), digitized from Figures 5-8 of Keller et al. (1979). The red curve in Figure 10 is the extracted resistivity from the 3D MT inversion model generated from fitting the 68 MT sites on Kīlauea. The inversion started from a 100 Ωm half-space (green line in Figure 10). Starting models of 10 and 200 Ωm half-spaces as well as a linear gradient from 1000 at the surface to 10 Ωm at -1 km elevation were tried as well. Within our sensitivity volume, the starting model had little effect on the final resistivities. The inversion has increased the resistivity in the upper 400 m from the start and lowered it below 400 m from the surface. The steepest resistivity gradient occurs in the vicinity of the sharp drop in resistivity with depth at the water table. The water table in the well is at an elevation of 650 m (491 m from the surface). In general, the inversion model has captured the trend in resistivity with depth but has underestimated the resistivity at depth compared to the logged values. From -100 m to the bottom of the log, where the minimum resistivities exist, the MT inversion predicts a lower resistivity than the log by a factor of approximately 3. This factor is in the opposite direction from that found on the synthetic models, where the average inverted resistivities were approximately

0.5 times higher than the true model values. The cause of the lower inverted resistivities compared to the log at depth could be due several factors in isolation or in combination: the drilling operations most likely cooled the formation raising the measured resistivity, the log is sampling a few meters around the well, whereas the inversion is sampling hundreds of meters, and Gibbs oscillations, as discussed in the model inversion section, could drive the inverted resistivities lower than the log.

7.2 3D MT inversion of the field data

All field data inversion plots define the sensitivity region as was done for the synthetic model inversions to shade areas of the model with expected low sensitivity. Figure 11a shows a plan view at -1 km elevation with the -9 km elevation view shown in Figure 11b. The traverse down the middle of the Ryan (1988) defined rift zones is shown in Figure 11c, and the southwest to northeast traverse is shown in Figure 11d. The distribution of low resistivity material is not uniform as it was in the synthetic model. Rather, there are three distinct areas of low resistivity that are within regions where the MT sites provide sensitivity. The first is beneath and slightly south of the Kīlauea caldera where the average resistivity is 6.2 Ωm. The second conductive anomaly lies in the Hilina fault system to the south-southwest of the caldera, with an average resistivity of 7.4 Ωm. The Hilina fault system extends to the east where there are three MT sites (between easting 265 and 272 km Easting) and the in situ resistivities are on the order of 100 Ωm. The final anomaly lies beneath and to the south of Puʻuʻōʻō with an average resistivity of 6.0 Ωm. The polygons that define the lateral extent of the volume used for averaging are shown in white on Figure 11a. The averaging elevation intervals are based on the depth intervals of the low resistivity anomalies and are -0.32 to 1.6 km for Kīlauea, -0.29 to 1.7 km for Puʻuʻōʻō, and 0.46 to 3.0 km for the Hilina fault system.

Based on the results of the synthetic model, we assume the resistivities in the most conductive zones at Kīlauea, Puʻuʻōʻō, and the Hilina fault zone are lower than the inversion predicts by 0.52, 0.45, and 0.52 respectively. This would mean the in situ resistivities in the conductive regions of the MT field data inversion would be 3.21 Ωm beneath Kīlauea, 2.7 Ωm beneath Puʻuʻōʻō, and 3.8 Ωm in the Hilina fault zone. At the time the MT data were taken (2002 – 2003), Puʻuʻōʻō was erupting, so the low resistivity material seen from 0 to -2 km elevation beneath and to the south of Puʻuʻōʻō most likely represents a spatial averaging of highly conductive magma and more resistive solidified surrounding rock. The low resistivity material, seen in Figures 11a, 11c, and 11d in the 0 to –2 km elevation range beneath and to the south of the Kīlauea caldera corresponds to the interpreted summit magma reservoir (e.g., Thurber, 1984, 1987; Rowan and Clayton, 1993; Dawson et al., 1999). While the resistivity of pure molten magma (melt) shown in Figure 2 would be between 0.5 and 2 Ωm depending on temperature, the MT inversion is seeing volume averages on a scale of kilometers. Thus, the inversion would resolve higher resistivities if the magma is present in fracture systems or smaller scale conduits where the surrounding rock is solid and thus resistive.

The earthquake hypocenters estimated by Lin et al. (2014a) are overlain on the inversion sections of Figure 11 as black-rimmed white dots. Only hypocenters within the time range 2001 thru 2004 are used. Those within 2 km perpendicular distance from the section lines are plotted on

Figure 11c and 11d. Those within +- 2 km of the constant elevation slice are plotted on Figure 11a and Figure 11b. Figures 11c and Figure 11d shows a concentration of hypocenters along planes that dip gently to the south-east between -2 and -3 km elevation in Figure 11c and to the north-east in figure 11d. Additionally, there is a column of hypocenters beneath Kīlauea in the elevation range from -5 to -15 km between 15 km and 20 km horizontal distance on the traverses. Earthquakes in volcanic areas have many sources, brittle-ductile transitions are one. Hence, hypocenters are commonly seen at the brittle-ductile transition (Ogawa et al., 2014). Beneath Kīlauea in the 1 km to -2 km elevation range, Lin et al. (2014a) shows areas of laterally extensive hypocenters that are parallel with Vp contours where Vp is increasing with depth. These areas correspond to increases in resistivity, such as seen in Figure 11c around -2km elevation. The hypocenters in the upper 3 km mainly lie near the 10 Ωm contour in the inverted resistivity models. Below -4 km elevation, the MT resistivity does not have the resolution to image resistivity contrasts that would be associated with brittle-ductile transitions.

The deeper hypocenters (-6 to -11 km elevation) seen in Figures 11c and 11d lie just to the northeast of the crest of a resistivity high beneath Kīlauea. This seismogenic zone has an approximately circular cross-section with a diameter of 4 km or less. According to Tilmann et al. (2001), “The vertical column is most plausibly explained as a conduit made up of disconnected and interconnected pockets of melt”. Within the conduit, the seismically active zone seems to vary somewhat as a function of time, suggesting that the precise pathways of the magma may occasionally shift (Ryan, 1988).

The broad anticline in higher resistivity beneath Kīlauea seen in the inversion may be caused by a resistive core, formed by multiple previous pathways that are now solidified, surrounding the most recent conduit to the mantle. If the conduit is indeed "disconnected and interconnected pockets of melt" as suggested by Tilmann et al. (2001) that are thin and on the order of 10s to 100s of meters, then MT would see a much larger volume average resistivity, and the thin melt zones would not show up as conductive zones at elevations below -4 km. High resistivity regions, such as the resistive anticline structure seen in Figure 11c and Figure 11d below ~ -3 km elevation, exclude the MT electric currents and hence reduce the sensitivity to conductivity details within. This results in the inability to resolve resistivity transitions associated with the brittle-ductile transition that would exist at the deep earthquake hypocenters.

Drawing conclusions about the geometry of the summit conduit complex is difficult since the entire island is built of mafic intrusive and extrusive flows, which are all expected to be highly resistive. Sensitivity to a resistive conduit complex at depth is also complicated by the high conductance of the upper 2 km of material which strongly reduces MT sensitivity to structure beneath the top 2 km. Such masking by near surface conductivity is a common occurrence e.g., Prichard et al. (2018). A comparison of the 4-14 km resistive anomaly beneath Kīlauea in the field data inversion and the synthetic model inversion does show significantly more resistive material beneath the summit than our synthetic model assumed.

7.3 Comparison of 3D MT resistivity and tomographic velocity models

A tomographic velocity model was constructed beneath Kīlauea by Dawson et al. (1999). The earthquake data used were concentrated in time, with eighty percent of the seismicity occurring on a single day, February 1, 1996 (Dawson et al., 1999). These published results are the closest in time to our MT acquisition (2002 – 2003). We also compare the MT resistivities to the velocity model derived by Lin et al. (2014a). Both studies used the HVO seismic network data but for different time periods. Dawson's study was augmented by data from a network of broadband seismometers within the summit caldera and a temporary array of stations centered on the southern boundary of the caldera synchronized with HVO for about three weeks in January 1996. Lin et al. (2014a) used seventeen years of HVO data between 1992 and 2009. Hence, the Dawson model is basically a high-resolution snapshot of the upper 4 km near Kīlauea caldera, while the Lin model is a lower-resolution time-average of seventeen years of activity over a much larger area with its maximum resolution in the -6 to -9 km elevation range (Lin et al., 2014a).

Dawson et al. (1999) constructed two traverses that go through the high station density portion of our MT survey, at and to the south of the Kīlauea caldera. We have used the Vp/Vs color scale convention with low Vp/Vs blue and high Vp/Vs red from the Dawson et al. (1999) figures, but it is noted that the resistivity color scales are flipped, with red for low resistivity and blue for high resistivity. This choice of color scales represents potential magma as red for high Vp/Vs and low resistivity. The locations of two Dawson et al. (1999) transects are shown as A- H-A' and B-H-B' in Figure 1. Figure 12 shows the 3D inverse resistivity along with the Vp and Vp/Vs models from Dawson et al. (1999). Figure 12a shows the 3D resistivity along the A-H-A' traverse with the earthquake hypocenters from 2001 through 2004 that occur within 2 km of the section from Lin et al. (2014a) overlaid. Figure 12b shows the digitized Vp taken from Figure 3a of Dawson et al. (1999) with contours of the 3D resistivity overlaid. There is an extremely high degree of correlation between the shape of the low resistivity anomaly and the Vp anomaly. The dip from west to east of the low resistivity zone closely matches the dip in the low Vp zone. Figure 12c shows the resistivity along the B-H-B' traverse, with Figure 12d showing the Vp/Vs digitized from Dawson et al. (1999) Figure 3b with the resistivity contours from Figure 12c overlaid. Again, a high degree of spatial correlation between the Vp/Vs and low resistivity anomalies is seen both in the west to east dip of the structure as well as the two lobes of low resistivity and high Vp/Vs (Figure 12d). Additionally, the 3D resistivity structure seen in Figure 12a and Figure 12c are consistent with the high-low-high resistivity versus depth of the 1D resistivity structures constructed by Kauahikaua (1982) from controlled source EM sounding along transects A-A' and C-C' (Kauahikaua, 1982, Figures 45 & 47).

The near-surface (surface to -1km elevation) areas within the caldera have low Vp associated with hydrothermal effects; just to the south of the caldera, a ring fracture system and a region of thick tephra and ash deposits is associated with low Vp as well (Dawson et al., 1999). The near surface resistivity within the caldera is low (Figure 12a and c), where hydrothermal activity would account for these lower resistivities. To the south (2 to 5 km distance on Figure 12c), the resistivity is high in the area of ring fractures and thick tephra and ash deposits. The volume of high Vp/Vs and low resistivity in the upper 3 km shown in Figure 12, centered beneath the southern caldera rim, coincides with the inferred summit magma reservoir derived from surface tilt measurements (Dvorak and Okumura, 1987; Dawson et al., 1999). The Vp/Vs values indicate that the shear velocities in the upper four kilometers beneath the southern portion of Kīlauea are anomalously low. The corresponding Poisson's ratio in the anomalous regions approach 0.32

(Dawson et al., 1999). This value suggests the presence of either highly fractured material and/or a significant fraction of partial melt (Dawson et al., 1999). The strong correlation between high Vp/Vs and low resistivity in the location of the summit magma reservoir suggests the low resistivity beneath Kīlauea represents significant fraction of partial melt. The melt fraction is estimated in section 7.4 below. From Figure 2, pure melt would have resistivities near 1 Ωm or less, depending on the temperature, so the inverted average values of 6.2 Ωm with a 0.52 correction factor would mean an in situ resistivity of 3.2 Ωm. This would be consistent with a volume average of melt and solidified rock.

The hypocenters used by Dawson et al. (1999) are shown as the small circles in the original Figures 3a and 3b from Dawson et al. (1999) and digitized in Figures 12b and 12d. They are different, both in quantity and location, from those generated by Lin et al. (2014a) that are shown in Figures 12a and 12b. The Dawson et al. (1999) hypocenters correlate with the two lobes of low resistivity material while the Lin et al. (2014a) hypocenters lie along the 30-40 Ωm contour from B to H but lie along the 10-20 Ωm contour from H to B' (Figure 12c). If the hypocenters should lie at a brittle-ductile transition, then the alignment of the locations of Lin et al. (2014a) events nearly along resistivity contours would suggest their locations are more consistent with the resistivity model than those of Dawson et al. (1999). We do not have the individual times for the events shown; thus, temporal differences could account for some of the location differences with differences in the velocity models and algorithms used accounting for the rest.

Courtesy of Guoqing Lin, a digital copy of the Vp and Vp/Vs models from Lin et al. (2014a) was used for comparison with the 3D MT model. While the model of Dawson et al. (1999)

is spatially limited to the area around Kīlauea caldera, the Lin et al. (2014a) model extends over the entire range of the MT survey.

Comparing the MT resistivity model shown in Figure 13a and 13b with the Lin et al. (2014a) Vp/Vs model shown in Figure 13c and 13d we see that the Vp/Vs model has larger spatial wavelength than the resistivity model. This is particularly true as the depth from the surface increases. From 20 km to 23 km distance Lin et al. (2014a) shows high Vp/Vs. This corresponds to the eastern side of the summit magma reservoir, where high Vp/Vs correlates with the low resistivity from the MT inversion. To the west, in the upper 3 km at 25 km distance (Figure 13c), there is a low Vp/Vs zone with low Vp (not shown) that is spatially correlated with a zone of moderate (~ 50 Ωm) resistivity. Low Vp and Vp/Vs can be associated with the presence of fluids (Lin et al. 2014a). Ground water filled porosity and/or fractures would be associated with resistivities higher than that of magma (1-5 Ωm) and lower than that of basalt (100-1000 Ωm). This area of low Vp, low Vp/Vs, and moderate resistivity (10-50 Ωm) could represent an area with ground water filled fractures. In general, within the upper 3 km from the surface, Vp/Vs varies laterally more quickly than does the resistivity. Areas of low Vp/Vs are often coincident with moderate resistivity, which would be consistent with areas of fluid-filled fractures in the near surface.

Near Pu‘u‘ō‘ō the transect shown in Figure 13a and Figure 13c just captures the northern edge of a high Vp/Vs anomaly to the west of Pu‘u‘ō‘ō at a distance of 34 km, that is seen in the -1 km elevation slice shown in Figure 13e. The high Vp/Vs anomaly is centered at easting 277 km and northing 2142 km where the Vp/Vs is 1.81 and the averaged inverted resistivity is 6.0 Ωm with a corrected in situ resistivity of 2.7 Ωm. The spatial correlation between the 5 Ωm contour in Figure 13e and high Vp/Vs seen on the -1 km elevation slice (Figure 13e) is quite good. These resistivity values are slightly lower than the 3.2 Ωm in situ resistivity seen for the magma chamber beneath Kīlauea. Given the spatial correlation with the high Vp/Vs from the Lin et al. (2014a) model, we interpret this anomaly as representing melt or partial melt feeding the eruption at Puʻuʻōʻō through a system of fractures in the upper 1 km below the surface. The feeder fractures are likely too thin to be captured in either the resistivity or the Vp/Vs model in the upper 1 km. It is also possible that the low resistivity seen over a larger area beneath Puʻuʻōʻō represents a combination of magma conduits and fluid-filled fracture zones, both of which would produce low resistivities.

On the southwest to northeast transect, the correlation between low resistivity and low Vp/Vs with low Vp (not shown) in the upper 4 km is better than on the rift zone transect. Directly beneath the caldera near sea level (0 elevation) at 17 km distance on Figure 13d there is an area of elevated Vp/Vs and low resistivity which would represent the summit magma reservoir (elevation 0 km to -2 km). To the south, centered beneath the southernmost MT site (Figure 13b), in the Hilina fault system, lies a low Vp/Vs (and low Vp) and low resistivity zone, which could represent a fluid filled fracture zone within the Hilina fault system.

Visual inspection of Figure 13a and Figure 13c shows an approximate demarcation between low resistivity and low Vp/Vs in the shallow section and high resistivity and high Vp/Vs in the deep section. The resistivity seen in Figure 13a and Figure 13b shows that in the -4 to -12 km elevation range, high resistivity correlates with high Vp/Vs anomalies in the Lin et al. (2014a) model, although the Vp/Vs model has larger spatial variations than is present in the resistivity. This would be consistent with the more rapid loss of resolution with depth with EM techniques compared to seismic. Lin et al. (2014b) proposes that the high Vp/Vs anomaly from -8 to -11 km elevation at bend point 4 (distance 25 km) in Figure 13c represents a crustal magma chamber. The resistivity model at this elevation (Figure 13a) shows only high resistivity.

Additional work to try and resolve the proposed deep magma chamber of Lin et al. (2014b) was done using the Vp/Vs model of Lin et al. (2014a). This is described in Supplement 2.

To summarize, in the upper 2-3 km from the surface, there is a high degree of correlation between MT derived resistivity and seismic derived Vp/Vs when, as is the case for Dawson et al. (1999), the seismic network provides high spatial coverage of the near-surface, and the MT station density is high (Figure 12). In areas where the combination of seismic receiver array and seismic events produce low sensitivity to the near-surface (low seismic ray count in the near surface) as is the case with Lin et al. (2014a) and the MT station density is low, the correlation between MT derived resistivity and seismic Vp/Vs is worse (Figure 13). Zhang et al. (2016), where the seismic array was aimed to image the lithosphere and upper mantle, shows a similar large-scale correlation but poorer fine-scale correlation in the near-surface.

7.4 Melt fraction from MT resistivities

The calculation of melt fraction from inverted MT resistivities requires several parameters whose values can be poorly constrained. The specific parameters depend on the method used. Here we follow the workflow of Zhang et al. (2016) and use the Hashin-Shtrikman upper bound (Hashin and Shtrikman, 1962) on the bulk conductivity formula for melt fraction θ:

$$\theta = \frac{3\sigma_M(\sigma_B - \sigma_S)}{(\sigma_B + 2\sigma_M)(\sigma_M - \sigma_S)}, \tag{1}$$

where σ_B, σ_M, and σ_S are the bulk, melt, and solid mantle conductivities, respectively. The solid mantle conductivity, σ_S, follows Wang et al. (2008) and is given as a function of temperature, T, iron content, X_{Fe}, water content C_w, and the gas constant R by:

$$\sigma_S = 10^{5.2} {C_w}^{0.67} exp\left(-\frac{183}{RT}\right) exp\left(X_{Fe}\frac{79}{RT}\right). \tag{2}$$

The bulk conductivity, σ_B, comes from the average conductivity in the inverse anomalous bodies, corrected by the results of the inversions of synthetic models. These are 3.2 Ωm beneath Kīlauea and 2.7 Ωm beneath Puʻuʻōʻō. The melt conductivity, σ_M, comes from the Silicate melts tab of the SIGMELTS web portal (Pommier and Le-Trong, 2011), which requires five parameters: Na_2O weight %, SiO_2 weight %, iron weight %, X_{Fe}, Temperature, Pressure, and water content as weight percent. Na_2O wt% and SiO_2 wt% are taken as 2.25 and 50.43 from averages of recent Kīlauea lavas from Table 5 of Wright (1971). X_{Fe} is taken as 0.1 from Yang et al. (2008). Pressure is taken as lithostatic pressure for 3.2 kg/m^3 overburden down to the center of anomalous bodies considered. The conductive bodies beneath Kīlauea and Puʻuʻōʻō lie between 5-10 km and 35-40 km horizontal positions, respectively in Figure 11c. Water content is taken from Moore et al. (2021) as 0.7 wt% for recent Kīlauea lavas. Calculations for melt fraction for a range of water content and temperature are shown in Figure 14. The conductive region beneath Kīlauea with a center depth 2.3 km below the surface and lithostatic pressure of 71 MPa are shown as solid lines. The conductive region beneath Puʻuʻōʻō with a center depth 1.6 km below the surface and lithostatic pressure of 49 MPa are dashed lines.

The temperature within the magma chambers inferred from the low resistivity bodies beneath Kīlauea and Puʻuʻōʻō is an uncertain parameter. For Kīlauea we use 1200 ^{o}C (U.S. geological Survey Hawaiian Volcano Observatory, 2017) for the temperature of the source magma at Kīlauea. At 1200 ^{o}C and 0.7 wt% water saturation (red curves in Figure 14) the calculated melt fraction is 0.096 and 0.117 for the Kīlauea magma chamber and Puʻuʻōʻō, respectively. For Kīlauea with 0.7 wt% the melt fraction varies with temperature from 0.14 to 0.057 for temperature 1150 to 1250 ^{o}C and for Puʻuʻōʻō from 0.17 to 0.074 for temperatures from 1150 to 1250 ^{o}C. Variations in melt fraction with water content for Kīlauea very from 0.11 to 0.094 for C_w from 0.1 to 1.0 at 1200 ^{o}C. For Puʻuʻōʻō melt fraction varies between 0.13 and 0.12 for C_w from 0.1 to 1.0 at 1200 ^{o}C. Comparing the melt fraction predicted from the two bulk resistivities at Kīlauea and Puʻuʻōʻō (3.2 Ωm and 2.7 Ωm), respectively, gives an idea of the sensitivity of the calculated melt fraction to bulk resistivity estimates, a 15% decrease in σ_B produces a 18% increase in predicted melt fraction. Examining all the variations in predicted melt fraction with reasonable variations in the input parameters suggest that the melt fractions derived from inverted MT resistivity and the assumed parameter values in the rock physics models yield a rough estimate of a 10% melt fraction beneath Kīlauea and Puʻuʻōʻō. While we were not able to find melt fraction estimates for the Kīlauea or Puʻuʻōʻō magma chambers in the literature, Lin et al. (2014b) predicts 10% melt in the "cumulate magma mush" for the proposed deep magma body between 9-11 km depth (Figure 13c, horizontal distance 25 km). Given all the uncertainties in these calculations (both seismic and MT) we conclude that the predicted melt fractions are consistent with Lin et al. (2114b).

8.0 SUMMARY AND CONCLUSIONS

We present the successful acquisition and interpretation of MT data for Kīlauea, Puʻuʻōʻō, and the East and Southwest rift zones using multi-station robust processing techniques and 3D modeling and inversion. Experimental challenges included confronting extremely high surface contact resistances and the need to install magnetic field coils covered only by sandbags–necessary to include fresh lava flows among the site installations. Logistical issues included highly variable climate, topography, vegetation, and site access. From a data acquisition perspective, MT data quality depends on several factors, including the length of recording time, the number of magnetic channels available at other sites, and the local levels of EM noise. To obtain accurate surface impedance measurements, and consequently accurate apparent resistivities and phase estimations, data needed to be acquired from at least three independent stations simultaneously. To minimize noise, the use of multi-station robust processing allowed using as many channels as recorded at one time. Data from stations accessed by helicopter were recorded with the E-fields only to reduce weight, setup time, and other logistical issues. Measurement stations employing helicopter data only were processed with and without local H-field data, and their intercomparisons (Supplement 1) demonstrate the validity of using remote H fields with local E fields for impedance calculations at low frequencies.

Synthetic modeling has shown that the MT data can resolve conductive bodies to a depth of 3 km (~ 2 km BSL) below the surface in the vicinity of MT sites. The synthetic models demonstrate that inverted resistivities, when averaged over the volume of structures of interest (Kīlauea and Puʻuʻōʻō magma chambers), need to be multiplied by approximately 0.5 to match in situ resistivities. Modeling also demonstrates that having the full range of frequencies (as compared to the actual field frequencies) at all the sites could significantly improve resolution in the rift zones.

The field data inversions indicate three anomalous conductive zones in the upper 3 km. One beneath Kīlauea caldera, a second approximately 15 km south of the caldera, and a third beneath and to the south of Puʻuʻōʻō. The conductive anomalies beneath Kīlauea are highly correlated with Vp/Vs anomalies found by Dawson et al. (1999) and indicate that in situ resistivities of 2 to 3 Ωm would be consistent with a partial melt or a volume average of melt and solidified rock. The MT spatial distribution of derived resistivity structure is less consistent with the spatial distribution of Vp/Vs anomalies found by Lin et al. (2014a), but this is consistent with the stated depth resolutions of the Lin et al. (2014a) model. The second conductive anomaly found approximately 15 km south of the Kīlauea caldera corresponds to the location of the Hilina fault system and thus may represent saline fluids within the fractures. To the east, within the same fault system, the resistivity is higher indicating that some portions of the fault system may be filled with fresh water. The third conductive anomaly beneath Puʻuʻōʻō, in the elevation range from 0 to -1 km, is most likely associated with magma within feeder fractures to the surface since Puʻuʻōʻō was erupting at the time of acquisition. The feeders to the Puʻuʻōʻō event do not show up as conductive or high Vp/Vs from 0 km elevation to the surface in either the MT resistivity or Lin et al. (2014a) models, probably due to their dimensions being below resolution of either technique.

Melt fraction calculations using the inverted average conductivity for bodies beneath Kīlauea and Puʻuʻōʻō using the workflow outlined by Zhang et al. (2016) predict 0.096 and 0.117 for the Kīlauea and Puʻuʻōʻō magma chambers respectively.

Constraining the resistivity model by the cross-gradients of the Lin et al. (2014a), Vp/Vs model in the inversion (Supplement 2) produces a model which lowers the resistivity around the location of the Lin et al. (2014b) proposed magma chamber. Forward modeling showed a small but consistent decrease in apparent resistivity at the lower frequencies. Hence the fact that the constrained inversion reduced model resistivity around the proposed magma chamber is tentative evidence of the existence of conductivity in this area. The demonstration of the algorithm opens the door to future joint inversion of the seismic travel-time and MT data which could possibly provide an improved model.

The results presented here demonstrate that accurate MT data can be acquired in the challenging environment of Hawaiian volcanos and can provide resistivity models that can be used to map the structures of the Kīlauea volcano. Advances in MT, particularly capacitive electrodes, inversion algorithms, and the cost of large-scale computing since this data was acquired should allow significant improvement in the application of MT as well as controlled source EM techniques coupled with other geophysical techniques for studying the internal structures of volcanoes in general and Kīlauea in particular.

9.0 ACKNOWLEDGMENTS

Support for this work was provided by the U.S. Department of Energy under Contract No. DE–AC03–76SF00098. We thank the staff of the Hawaiian Volcano Observatory of the U.S. Geological Survey, U. S. Department of the Interior, for logistical and personnel support, where Arnold T. Okamura helped in many ways. Dallas Jackson provided correspondence and helpful advice. Michael P. Ryan of the USGS provided many helpful discussions. Paul Bedrosian of the USGS provided many helpful comments and suggestions in the reviewing this work. We are grateful for the contributions of equipment and personel to the data acquisition program by ElectroMagnetic Instruments Inc. Helicopter support was provided by Volcano Helicopters/David Okita. We also thank Heidi Anderson, Sierra Boyd, Bruce Chuchel, Ramsey Haught, Edward Nichols, and Chester Weiss for their help with data acquisition. Experiments were conducted within the Hawai'i Volcanoes National Park, U.S. National Park System, U.S. Department of the Interior.

10.0 DATA AVALIBILITY STATEMENT

The processed MT impedances for each site collected on Kīlauea volcano are available from OpenEI Geothermal Data Repository. https://dx.doi.org/10.15121/1872965.

11.0 SOFTWARE AVAILABILITY STATEMENT

The 3D MT inversion software use in the paper is CGG proprietary commercial software and is not publicly available.

12.0 REFERENCES

Aizawa K, Koyama T, Hase H, Uyeshima M, Kanda W, Utsugi M, Yoshimura R, Yamaya Y, Hashimoto T, Yamazaki K, Komatsu S, Watanabe A, Miyakawa K, Ogawa Y. (2014), Three-dimensional resistivity structure and magma plumbing system of the Kirishima volcanoes as inferred from broad-band magnetotelluric data. Journal of Geophysical Research, **119**, 1–18, doi:10.1002/2013JB010682

Backus, G.E., Gilbert, J.F. (1968), The resolving power of gross earth data. Geophys. J. R. Astron. Soc., **16**, 169-205.

Bartel, L.C., and Jacobson, R.D. (1987), Results of a controlled source audiofrequency magnetotelluric survey at the Puhimau thermal area, Kīlauea Volcano, Hawai'i. Geophysics, **52**, 665-677.

Bayrak, M., Ilkisik, O.L., Kaya, C., and Basokur, A.T. (2000), Magnetotelluric data in western Turkey: Dimensionality analysis using Mohr circles. Journal of Geophysical Research, **105**, B10, 23,391-23,401.

Bigalke, J. (2000), Derivation of an equation to calculate the average conductivity of random networks. Physica A, **285**, 295-305.

Cagniard, L. (1953), Basic Theory of the Magnetotelluric Method of Geophysical Prospecting. Geophysics, 18, 605-635. doi:10.1190/1.1437915

Cervelli, P.F., and Miklius, A. (2003), The shallow magmatic system of Kīlauea Volcano, in Heliker, C., Swanson, D.A., and Takahashi, T.J., eds., The Pu‘u ‘Ō‘ō-Kūpaianaha eruption of Kīlauea Volcano, Hawai‘i; the first 20 years. U.S. Geological Survey Professional Paper 1676, 149–163. http://pubs.usgs.gov/pp/pp/1676/.

Chouet, B.A., Dawson, P.B., James, M.R., and Lane, S.J. (2010), Seismic source mechanism of degassing bursts at Kīlauea Volcano, Hawaii; results from waveform inversion in the 10–50 s band. Journal of Geophysical Research, **115**, B09311, 24 p., doi:10.1029/2009JB006661

Clemens, M., and Weiland T. (2001), Discrete electromagnetism with the finite integration technique. Progress In Electromagnetics Research, **32**, 65–87.

Comeau, M.J., Unsworth, J., and Cordell, D. (2016), New constraints on the magma distribution and composition beneath Volcan Uturuncu and the southern Bolivian Altiplano from Magnetotelluric data. Geosphere, **12**(5), 1391-1421.

Constable, S. and Weiss, C. (2006), Mapping thin resistors and hydrocarbons with marine EM methods: Insights from 1D modeling. Geophysics **71**(2), G43-G51.

Daniels, K.A., Kavanagh, J.L., Menard, T., and Sparks, R.S.J. (2012), The shape of dikes; evidence for the influence of cooling and inelastic deformation. Geological Society of America Bulletin, **124**, nos. 7–8, 1102– 1112, doi:10.1130/B30537.1.

Day, S. J., Heleno da Silva, S.I.N., and Fonseca, J. F. B. D. (1999), A past giant lateral collapse and present-day flank instability of Fogo, Cape Verde Islands. J. Volcanol. Geotherm. Res., **94**, 191– 218.

Dawson, P.B., Chouet, B.A., Okubo, P.B., Villasenor, A., and Benz, H.M. (1999), Three-dimensional velocity structure of the Kīlauea caldera, Hawaii. Geophysical Research Letters. **26**, N0.18, 2805-2808.

Delaney, P.T., Miklius, A., Arnadottir, T., Okamura,A.T., and Sako, M.K. (1993), Motion of Kīlauea volcano during sustained eruption from the Pu'u O'o and Kupaianaha vents, 1982-1991. Journal of Geophysical Research. **98**, 17,801-17,820.

Dvorak, J.J,and Dzurisin D. (1997), Volcano geodesy: The search for magma reservoirs and the formation of eruptive vents. Reviews in Geophysics. **35**, 343-384.

Dvorak, J.J. and Okamura A.T. (1987), A hydraulic model to explain variations in summit tilt rate at Kīlauea and Mauna Loa volcanoes. *in* (Decker, R.W., T.L. Wright, and P.H. Stauffer, Eds.) *Volcanism in Hawaii.* Vol. II. U.S. Geological Survey Professional Paper 1350, 1281-1296.

Egbert, G.D. (1997), Robust multiple station magnetotelluric data processing. Geophysical Journal International **130,** 475-496.

Farquharson, C.G. and Oldenburg, D.W. (1996), Approximate sensitivities for the electromagnetic inverse problem. Geophysical Journal International **126**, 235-252.

Gallardo, L. A., and Meju, M.A. (2003), Characterization of heterogeneous near-surface materials by joint 2D inversion of dc resistivity and seismic data. Geophysical Research Letters, **30**, 1658.

Gallardo, L.A., and Meju, M.A. (2004), Joint two-dimensional dc resistivity and seismic travel-time inversion with cross-gradients constraints. Journal of Geophysical Research, **109**, B03311.

Gamble, T.D., Goubau W.M., and Clarke, J. (1979), Magnetotellurics with a remote reference. Geophysics. **44**, 53-68.

Gibbs, J. W. (1898), Fourier's Series, Nature, **59** (1522): 200, doi:10.1038/059200b0, ISSN 0028-0836, S2CID 4004787

Hashin, Z., and Shtrikman, S. (1962), A variational approach to the theory of the elastic behavior of polycrystals. Journal of Mechanics and Physics of Solids, **10**, 343-352.

Haslinger F., Thurber, C., Mandernach, M., and Okubo, P. (2001), Tomographic image of P-velocity structure beneath Kīlauea's East Rift Zone and South Flank: seismic evidence for a deep magma body. Geophysical Research Letters, **28**,2, 375-378.

Hermance, J.F., and Colp, J.L. (1982), Kīlauea Iki Lava Lake: Geophysical constraints on its present (1980) physical state. Journal of Volcanology and Geothermal Research, **13**, 31-61.

Hibbs, A. D. (2014), Evaluation of deep subsurface resistivity imaging for hydrofracture monitoring. U.S. Department of Energy, National Energy Technology Laboratory, Fifth Quarterly Progress Report, Project Number: DE-FE0013902.

Hibbs, A. D., Petrov, T.R., Pendleton, J., Agundes, A., Kouba, S., Hall, T., Boyle, D., Martin, T., Schenkel, C. and Morrison, H.F. (2014), Advances in Electromagnetic Survey Instrumentation and the Use of a Cased Borehole for Imaging a Deep Formations. 76th EAGE Conference and Exhibition – Workshops, June 2014, cp-401–00120. doi:10.3997/2214-4609.20140562.

Hill G.J., Caldwell T.G., Heise W., Chertkoff, D.G., Bibby H.M., Burgess M.K., Cull J.P., Cas R.A.F. (2009), Distribution of melt beneath Mount St Helens and Mount Adams inferred from magnetotelluric data. Nat Geosci **2**:785–789, doi:10.1038/ngeo661.

Hoversten, G.M. (2003), Magnetotelluric Imaging of the Kīlauea Volcano, Hawaii, 73rd Ann. Internat. Mtg.: Soc. of Expl. Geophys., 2387-2390.

Hoversten, G.M., Mackie, R.L., Hua, Y. (2021), Reexamination of controlled-source electromagnetic inversion at Lona prospect, Orphan Basin, Canada. Geophysics, **86**(3), E157-E170, doi: 10.1190/geo2020-0538.1.

Ingham M.R., Bibby H.M., Heise W., Jones K., Cairns P., Dravitzki S., Bennie S.L., Caldwell T.G., Ogawa Y. (2009), A magnetotelluric study of Mount Ruapehu volcano, New Zealand. Geophysical Journal International. **179**, 887–904, doi:10.1111/j.1365-246X.2009.04317.x

Jackson, D.D. (1972), Interpretation of Inaccurate, Insufficient and Inconsistent Data. Geophysical Journal of the Royal Astronomical Society, **28**(2), 97-109. doi:10.1111/j.1365-246X.1972.tb06115.x

Jackson, D.B., Kauahikaua J., and Zablocki, C.J. (1985), Resistivity monitoring of an active volcano using controlled source electromagnetic technique: Kīlauea, Hawaii. Journal of Geophysical Research, **90**, B14, 12, 545-12, 555.

Kauahikaua, J. (1982), The subsurface resistivity structure of Kīlauea Volcano, Hawai'i: Ph.D. dissertation, University of Hawaii.

Kauahikaua, J., Jackson, D.B., and Zablocki, C.J. (1986), Resistivity structure to a depth of 5 km beneath Kīlauea Volcano, Hawaii, from large loop source electromagnetic measurements (0.04 to 8 Hz). Journal of Geophysical Research, **91**, B8, 8,267-8,283.

.

Keller, G.V., Grose, L.T., Murray J.C., and Skokan, C.K. (1979), Results of an experimental drill hole at the summit of Kīlauea Volcano. Hawaii. Journal of Volcanology and Geothermal Research. **5**, 345-385.

Klein, F.W., Koyanagi, Y., Nakata, J. and Tanigawa, W.. (1987), The seismicity of Kīlauea's magma system in (Decker, R.W., Wright, T.L., Stauffer, P.H. Eds) Volcanism in Hawaii. Vol. II U.S. Geological Survey Professional Paper 1350.

Lay T.; Ye L.; Kanamori H.; Satake K. (2018), Constraining the Dip of Shallow, Shallowly Dipping Thrust Events Using Long- Period Love Wave Radiation Patterns: Applications to the 25 October 2010 Mentawai, Indonesia, and 4 May 2018 Hawaii Island Earthquakes. Geophysical Research Letters, **45** (19): 10, 342–10, 349. doi:10.1029/2018GL080042

Li, Y., Thurber, C.H., and Munson, C.G. (1992), Profile of discontinuities beneath Hawaii from S to P converted seismic waves. Geophysical Research Letters, **19**(2), 111-114.

Lin, G., Shearer, P.M., Matoza, R.S., Okubo, P.G. and Amelung, F. (2014a), Three-dimensional seismic velocity structure of Mauna Loa and Kīlauea volcanoes in Hawaii from local seismic tomography. Journal of Geophysical Research: Solid Earth. **119** Issue 5, 4377-4392. doi:10.1002/2013JB010820

Lin, G., Amelung, F., Lavallee, Y., and Okubo, G. (2014b), Seismic evidence for a crustal magma reservoir beneath the upper rift zone of Kīlauea volcano, Hawaii. Geology **42**(3), 187–190. doi:10.1130/G35001.1

Lipman, P., Lockwood J., Okamura R., Swanson, D., and Yamashita K. (1985), Ground deformation associated with the 1975 magnitude-7.2 earthquake and resulting changes in activity of Kīlauea volcano, Hawaii. U.S. Geological Survey Professional Paper **1276**, 1–45.

Lundgren, P., Poland, M., Miklius, A., Orr, T., Yun, S.-H., Fielding, E., Liu, Z., Tanaka, A., Szeliga, W., Hensley, S., and Owen, S. (2013), Evolution of dike opening during the March 2011 Kamoamoa fissure eruption, Kīlauea Volcano, Hawai`i. Journal of Geophysical Research, **118**, 897–914, doi:10.1002/jgrb.50108.

Mackie, R.L. and Watts, M.D. (2012), Detectability of 3-D sulfide targets with AFMAG. SEG Technical Program Expanded Abstracts: 1-4.

Mackie, R.L., Meju, M.A., Miorelli, F., Miller, R.V., School, C., and Saleh, A.S. (2020), Seismic Image-Guided 3D inversion of Marine CSEM and MT data. Interpretation, **8**, SS1-SS13.

Massonnet, D. and Sigmundsson F. (2000), Remote sensing of volcano deformation by radar interferometry from various satellites. *in* (Mouginis-Mark, P.J., J.A. Crisp, and J.H. Fink, Eds.)

Remote Sensing of Active Volcanism. Geophysical monograph 116. American Geophysical Union. Washington, D.C. 207-221.

Matsunaga Y, Kanda W, Takakura S, Koyama T, Saito Z, Seki K, Suzuki A, Kishita T, Kinoshita Y, Ogawa Y. (2020a), Magmatic hydrothermal system inferred from the resistivity structure of Kusatsu-Shirane volcano. Journal of Volcanology and Geothermal Research. doi:10.1016/j.jvolgeores.2019.106742.

Matsunaga Y, Kanda W, Koyama T, Takakura S, Nishizawa T, (2020b), 3-D resistivity structure model around Kusatsu-Shirane volcano revealed by broadband magnetotellurics. Paper presented at the AGU Fall Meeting, Online, 1–17 December 2020.

Mavko, G., (1980), Velocity and attenuation in partially molten rocks, Journal of Geophysical Research, **85**, B10, 5173-5189.

Miensopust, M.P., Queralt, P., Jones, A.G., and the 3D MT modellers. (2013), Magnetotelluric 3-D inversion – a review of two successful workshops on forward and inversion code testing and comparison, Geophysical Journal International, **193**, 1216-1238, doi:10.1093/gji/ggt06.

Miklius, A., Cervelli, P., Sako, M., Lisowski, M., Owen, S., Segal, P., Foster, J., Kamibayashi, K., and Brooks, B. (2005), Global Positioning System measurements on the Island of Hawai`i; 1997 through 2004. U.S. Geological Survey Open File Report 2005–1425, 46 p. [Also available at http://pubs. usgs.gov/of/2005/1425/of2005-1425.pdf.]

Mogi, T. & Nakamura, S. (1993), Magnetotelluric interpretation of the geothermal system of the Kuju volcano, southwest Japan. Journal of Volcanology and Geothermal Research, **56,** 297–308.

Moore, L.R., Gazel, E., and Bodnar, R.J. (2021), The volatile budget of Hawaiian magmatism: Constraints from melt inclusions from Haleakala volcano, Hawaii. Journal of Volcanology and Geothermal Research, **410**, 107144.

Morgan, J. K., and Clague, D.A. (2003), Volcanic spreading on Mauna Loa volcano, Hawaii: Evidence from accretion, alteration, and exhumation of volcaniclastic sediments. Geology, **30**, 411 – 414.

Nettles, M., and Ekström, G. (2004), Long-Period Source Characteristics of the 1975 Kalapana, Hawaii, Earthquake. Bulletin of the Seismological Society of America, **94**(2), 422–429.

Nolasco, R., Tarits, P., Filloux, J.H., and Chave, A.D. (1998), Magnetotelluric imaging of the Society Islands hotspot. Journal of Geophysical Research. **103**, B12, 30,287-30,309.

Ogawa, Y., Ichiki, M., Kanda, W.. Mishina, M., and Asamori, K. (2014), Three-dimensional Magnetotelluric imaging of crustal fluids and seismicity around Naruko volcano, NE Japan. Earth, planets, and Space, **66**, 158.

Ogawa, Y., Bibby, H.M., Caldwell, T.G., Takakura, S., Uchida, T., Matsushima, N., Bennie, L., Tosha, T., and Nishi, Y. (1999), Wide-band magnetotelluric measurements across the Taupo volcanic zone, New Zealand: Preliminary results. Geophysical Research Letters, **26**(3), 673-676.

Okubo, P.G., Benz, H.M., and Chouet, B.A. (1997), Imaging the crustal magma sources beneath Mauna Loa and Kīlauea volcanoes, Hawaii, Geology, **25**(10), 867-870.

Owen, S., Segall, P., Freymueller, J., Denlinger R., Arnadottir T., Sako M., and Burgmann R., (1995), Rapid deformation of the south flank of Kīlauea Volcano, Hawaii. Science. **267**, 1328-1332.

Park, S. & Torres-Verdin, C. (1988), A systematic approach to the interpretation of magnetotelluric data in volcanic environments with applications to the quest for magma in Long Valley, California. Journal of Geophysical Research, **93(**B11), 13265-13283.

Poland, M.P., Miklius, A., Sutton, A.J., and Thornber, C.R. (2012), A mantle-driven surge in magma supply to Kīlauea Volcano during 2003–2007. Nature Geoscience, **5**(4), 295–300. (supplementary material, 16 p.), doi:10.1038/ngeo1426.

Poland, M.P., Mikilius, A., and Montgomery-Brown, E.K. (2014), Magma Supply, Storage, and Transport at Shield-Stage Hawaiian Volcanoes. chap. 5 *of*, Poland M. P., Takahashi, T.J., Landowsk, T., and Landowsk, C., *eds*., Characteristics of Hawaiian Volcanoes,U.S. Geological Survey Professional Paper 1801.

Pommier, A., Le-Trong, E. (2011), "SIGMELTS": a web portal for electrical conductivity calculations in geosciences. Computers & Geosciences, Elsevier, 2011, 37, pp.1450-1459. ff10.1016/j.cageo.2011.01.002ff. ffinsu-00563856

Rai, M.P., and Manghnami, M.H. (1977), Electrical conductivity of basalts to 1,550 OC, in H. Dick, ed., Magma Genesis, Proceedings of the American Geophysical Union Chapman Conference on Partial Melting in the Earth's Upper Mantle: Oregon Department of Geology and Mineralogy Bulletin, **96**, 219-232.

Rodi, W., and Mackie R.L. (2001), Nonlinear conjugate gradients algorithm for 2D magnetotelluric inversion. Geophysics, **66**, 174-187.

Rowan, L., and Clayton R.W. (1993), The three-dimensional structure of Kīlauea Volcano, Hawaii, from travel time tomography. Journal of Geophysical Research, **98**, 4355–4375.

Ryan, M.P. (1987), The elasticity and contractancy of Hawaiian olivine tholeiite, and its role in the structural evolution of subcaldera magma reservoirs and rift systems. *in* (Decker, R.W., T.L. Wright, and P.H. Stauffer, Eds.) *Volcanism in Hawaii.* Vol.II. U.S. Geological Survey Professional Paper 1350, 1395-1447.

Ryan, M.P. (1988), The mechanics and three-dimensional internal structure of active magmatic systems: Kīlauea Volcano, Hawaii. Journal of Geophysical Research. **93**(B5), 4,213-4,248.

Ryan, M.P., Koyanagi, R.Y. and Fiske, R.S. (1981), Modelling the three-dimensional structure of magma transport systems: Application to Kīlauea Volcano, Hawaii. Journal of Geophysical Research. **86**, 7,111-7,129.

Smith J.T., and Booker J. (1988), Magnetotelluric inversion for minimum structure. Geophysics, **53**(12), 1565-1576.

.

Smith B.D., and Frischknect, F.C. (1980), Progress report on 1980 electromagnetic experiments on Kīlauea Iki lava lake. Sandia National Laboratory, Albuquerque, N.M.

Soyer. W., Hallinan, S., Mackie, R.L., Pavesi, A., Nordquist, G., Suminar, A., Intani, R., and Nelson, C. (2018), Geologically-consistent multiphysics imaging of the Darajat geothermal steam field. First Break **36**(6), 77-83.

Takei, Y. (1998), Constitutive mechanical relations of solid-liquid composites in terms of grain-boundary contiguity, J. Geophys. Res., **103**, 18,183 – 18,203, doi:10.1029/98JB01489.

Tilling, R. I., R. Y. Koyanagi, P. W. Lipman, J. P. Lockwood, J. P. Moore, and Swanson D.A., (1976), Earthquake and related catastrophic events, island of Hawaii, November 29, 1975: A preliminary report. U.S. Geol. Surv. Circ., **740**, 33 pp.

Tilmann, F.J., Benz, H.M., Priestley, K.F., and Okubo, P.G. (2001), P-wave velocity structure of the uppermost mantle beneath Hawaii from traveltime tomography, Geophysical Journal International, **46**, 594-606.

Tseng K.H., Ogawa Y., Nurhasan, Tank S.B., Ujihara N., Honkura Y., Terada A., Usui Y., Kanda W. (2020), Anatomy of active volcanic edifice at the Kusatsu-Shirane volcano Japan, by

Magnetotellurics: hydrothermal implications for volcanic unrests. Earth Planet Space 72:161. doi:10.1186/s40623-020-01283-2.

Thurber, C. (1984), Seismic detection of the summit magma complex of Kīlauea volcano, Hawaii. Science, **223**, 165–167.

Thurber, C. H. (1987), Seismic structure and tectonics of Kīlauea Volcano. *in* (Decker, R.W., T.L. Wright, and P.H. Stauffer, Eds.) *Volcanism in Hawaii*. Vol. II. U.S. Geological Survey Professional Paper 1350, 919-934.

U.S. Geological Survey Hawaiian Volcano Observatory (2017), Volcano Watch – Magma: What's hot and what's not. November 9, 2017.

Wang, D., Li, H., Yi, L., Shi, B., 2008. The electrical conductivity of upper-mantle rocks: water content in the upper mantle. Physics and Chemistry of Minerals. 35, 157-162. doi:10.1007/s00269-007-0207-1.

Wannamaker P.E., Caldwell T.G., Jiracek, G.R., Maris V., Hill G.J., Ogawa Y, Bibby H.M., Bennie S.L., Heise H. (2009), Fluid and deformation regime of an advancing subduction system at Marlborough, New Zealand. Nature **460**, 733–736, doi:10.1038/nature08204

Ward, S. N. (2002), News and views: Slip-sliding away, Nature, **415**, 973–974.

Weiland, T. (1977), A discretization method for the solution of Maxwell's equations for six-component fields. Electronics and Communications AEÜ, **31**, 116–120.

Weiland, T. (1996), Time domain electromagnetic field computation with finite difference methods, International Journal Of Numerical Modelling: Electronic Networks. Devices and Fields, **9**, 295–319.

Wirgin, A. (2004), The Inverse Crime, arXiv:math-ph/0401050 **,** https://doi.org/10.48550/arXiv.math-ph/0401050

Wright, T.L. (1971), Chemistry of Kīlauea and Mauna Loa Lava in Space and Time, U.S. Geological Survey Professional Paper 735, 40 p.

Wright, T.L., and Klein, F.W. (2014), Two hundred years of magma transport and storage at Kīlauea Volcano, Hawai‘i, 1790–2008. U.S. Geological Survey Professional Paper 1806, 240 p., 9 appendixes. [Also available at http:// http://pubs. usgs.gov/pp/1806/.]

Wyss, M., F. Klein, K. Nagamine, and Wiemer S. (2001), Anomalously high *b*-values in the south flank of Kīlauea Volcano, Hawaii: Evidence for the distribution of magma below Kīlauea's East Rift Zone. Journal of Volcanology and Geothermal Research. **106,** 23-37.

Yang, X., Xia, Q., Deloule, E., Dallai, L., Fan, Q., Feng, M., (2008), Water in minerals of the continental lithospheric mantle and overlying lower crust: a comparative study of peridotite and granulite xenoliths from the North China Craton. Chemical Geology, **256**, 33–45. http://dx.doi.org/10.1016/j.chemgeo.2008.07.020.

Yang, B., Lin, W., Hu, X., Fang, H., Qin, G., and Wang, G. (2021), The magma system beneath Changbaishan-Tianchi Volcano, China/North Korea: Constraints from three-dimensional Magnetotelluric imaging. Journal of Volcanology and Geothermal Research, **419**: 107385.

Ye, T., Huang, Q., Chen, X., Zhang, H., Chen, Y.J., Zhao, L., and Zhang, Y. (2018), Magma Chamber and Crustal Channel Flow Structures in the Tengchong Volcano Area From 3-D MT Inversion at the Intracontinental Block Boundary Southeast of the Tibetan Plateau. Journal of Geophysical Research: Solid Earth, **123**, 11,112–11,126. https://doi.org/10.1029/2018JB015936

Yee, K. S. (1966), Numerical Solution of Initial Boundary Value Problems Involving Maxwell's Equations in Isotropic Media. IEEE Transactions on Antennas and Propagation, **AP-14**, 302–307.

Zablocki, C.J., Tilling, R.I., Peterson, D.W., and Christiansen, R.L. (1974), A Deep Research Drill Hole at the Summit of an Active Volcano, Kīlauea, Hawaii. Geophysical Research Letters **1**(7), 323-326.

Zebeker, H.A., Amelung F., and Jonsson S. (2000), Remote sensing of volcano surface and internal processes using radar interferometry. *in* (Mouginis-Mark, P.J., J.A. Crisp, and J.H. Fink, Eds.) *Remote Sensing of Active Volcanism*. Geophysical monograph 116. American Geophysical Union. Washington, D.C.179-205.

Zhang, H., Huang, Q., Zhao, G., Guo, Z., and Chen, Y.J. (2016), Three-dimensional conductivity model of crust and uppermost mantle at the northern Trans North China Orogen: Evidence for a mantle source of Datong volcanoes. Earth and Planetary Science Letters, **453**, 182-192.

Zohdy, A.A.R. and Jackson, D.B. (1969), Application of deep electrical soundings for ground - water exploration in Hawaii. Geophysics **34**, 584-600.

13.0 FIGURE CAPTIONS

Figure 1. MT survey locations (blue diamonds) on Kīlauea Volcano, Hawai‘i, and its primary rift zones. Major craters within the East rift zone are shown in red, as are some vents active during the Pu‘u‘ō‘ō series of eruptions after January 3, 1983. Major flows after 1983 are shown as shaded areas around Pu‘u‘ō‘ō. Sites described in the text are marked by filled blue diamonds, sites not described are open blue diamonds. The site at the 1973 Keller-NSF summit research drill hole is designated “Keller”. The Saddle remote site lies in the geomorphic saddle between Mauna Kea and Mauna Loa. The rift zones defined by Ryan (1988) at an elevation of -1 km are shown as the light gray region. Elevation contours are 0.5 km. Easting and Northing are UTM zone 5.

Figure 2. After Kauahikaua (1986). Expected variations in basalt resistivity are shown for temperatures from 20 to 1400 ^{o}C. The solid line shows the resistivity expected for completely dry rock; the two shaded areas show ranges of resistivities for typical basalts saturated with two different salinity (S) fluids. The two models are 1) ground water with ρ_w= 2 Ωm and S= 3 and 2) sea water with ρ_w =0.21 Ωm and S=35 ppm. The cusp in the curve for dry tholeiite is probably an effect of the speed of experimental heating and cooling (Rai and Manghnani, 1977) and is not significant for field survey interpretation. The arrow labeled “Melt” indicates the temperature range in which basalts are molten.

Figure 3. Synthetic Model for testing resolution of 3D MT inversion. The model has four features: 1) combined southwest and northeast rift zones at 1 Ωm, 2) a resistive conduit to the mantle at

1000 Ωm, 3) a possible deep magma chamber at 1 Ωm between -7.5 and -10.5 km elevation, and 4) Hilina fracture zone between elevations 0.2 and -2.0 km at 10 Ωm. The conductive rift zones top and base horizons run parallel to the surface elevation but are shifted down by 0.8 and 2.8 km respectively. The resistive conduit to the mantle extends from the base of the rift zones to 14.7 km below the surface. a) and b) show elevation slices at -1 and- 9 km respectively. Traverse along the center of the Ryan (1988) defined rift zones is shown in c). Southwest to northeast traverse is shown in d).

Figure 4. a) is the synthetic model (Model 1) elevation slice at -1 km (approximately 2 km below the surface). b) is the resistivity from 3D inversion of the synthetic data generated from Model 1. MT sites are shown as inverted green triangles. The outlines of the anomalous conductive bodies in the synthetic model are shown as white lines in a). Polygons used for averaging conductivity to derive correction factors are labeled P1 through P3 and are shown in black in a). The approximate resolution matrix values are contoured in black in b). The unshaded region of b) is the region where we expect sensitivity. The polygon defined by the black dashed line in b) is the line around the sites with a minimum distance of 2 km between the polygon and the sites. The 3D sensitivity region is defined as the union of the polygon and the volume where the resolution values are greater than 0.3.

Figure 5. Comparison of Synthetic Model 1 and inversion of data calculated over it. a) is the traverse along the center of rift zones in the synthetic model 1. b) is the SW to NE traverse through the synthetic model 1. c) is the traverse along the center of the rift zones in the 3D inversion of

synthetic data. d) is the SW to NE traverse through the 3D inversion of the synthetic data. The traverse bend points 1-6 shown on a) and c) and the SW and NE end points on b) and d) are shown in Figure 3 a) and c) for location. MT sites within a perpendicular distance of 2 km from the section lines are shown as inverted green triangles. The approximate resolution matrix values are contoured in black in c) and d). Only resolution values of 0.7 or less are plotted, higher values concentrate near surface around the MT sites and are not shown to avoid clutter. In c), and d), the area defined by resolution values < 0.3 and outside of the surface polygon around the sites, shown in Figure 4b, is shaded.

Figure 6. Data misfit break down by frequency a) and by site b). Upper panels show RMS and lower panels show the number of data samples. In b) the sites are ordered from west to east with the four selected for display in Figure 17 highlighted by red dots.

Figure 7. Real and Imaginary data fits from 4 sites. Sites are ordered from west to east and shown in Figure 6 for RMS misfit comparisons to other sites. Colors correspond to horizontal elements of the impedance tensor, red = XX, blue = XY, green = YX, and black = YY. Error bars are 1 standard deviation.

Figure 8. Comparison of 3D MT inversion results for model with the resistive conduit to the mantle (Model 1) a) and b) and the results for the model without the resistive conduit to the mantle (Model 2) c) and d). a) and c) are the traverse along the center of the rift zones. b) and d) are for the southwest to northeast traverse (see Figure 4 for location). MT sites within a perpendicular

distance of 2 km from the section lines are shown as inverted green triangles. The area defined by resolution values < 0.3 and outside of the surface polygon around the sites, shown in Figure 4b, is shaded.

Figure 9. Comparison of inversion for data set with all frequencies at all sites and data set with field acquisition frequencies. a) depth-section for traverse along center of rift zones from inversion with field acquisition frequencies at each site (Model 1). b) southwest to northeast depth-section from inversion with field acquisition frequencies at each site (Model 1). c) depth-section for traverse along center of rift zones from inversion with data with all frequencies at each site (Model 3). d) southwest to northeast traverse from inversion with all frequencies at each site (Model 3). The traverse bend points 1-6 shown on a) and c) and the SW and NE labels on b) and d) are shown in Figure 4 for location. MT sites within a perpendicular distance of 2 km from the section lines are shown as inverted green triangles.

Figure 10. Deep induction log from the NSF well on the southern flank of Kīlauea caldera. The black curve is digitized from Figures 5 – 8 of Keller et al. (1979). The red curve is the extracted resistivity from the 3D MT inversion model along the well trajectory. The water table elevation in the well is shown as the blue horizontal line. The starting model resistivity for the 3D inversion is shown as the vertical green line.

Figure 11. Four slices through the 3D MT inversion model. a) is the elevation slice at -1 km. The southwest to northeast and center rift zone traverses are shown as black lines, the Koaʻe and Hilina

fault systems are marked with magenta lines. Three white polygons in a) mark volumes used for conductivity averaging. b) is the elevation slice at -9 km. The MT sites are shown as green triangles. c) is a depth-section traverse along the center of a polygon defining the interpreted rift zones at -1 km elevation from Ryan (1988). d) is southwest to northeast depth-section through Kīlauea caldera. The black rimmed white dots are earthquake hypocenters from Lin et al. (2014a) within the time range 2001 thru 2004 that lie within 2 km perpendicular distance from the section lines (c and d) and between the surface and -2 km elevation for the -1 km elevation slice and between -7 and -11 km elevation for the 9 km elevation slice. The black contour lines are constant values of the approximate resolution matrix. Areas below resolution value of 0.3 or outside of the polygon around the MT sites are shaded.

Figure 12. Comparison between the 3D MT inversion and published Vp and Vp/Vs models from Dawson et al. (1999). a) is the 3D resistivity inversion on transect A-H-A’ of Dawson et al. (1999) with contours of approximate resolution matrix overlaid. b) is the Vp digitized from Figure 3a of Dawson et al. (1999) with contours of resistivity from a) overlaid. c) is the 3D resistivity inversion from transect B-H-B’ of Dawson et al. (1999) with contours of approximate resolution matrix overlaid. d) is the Vp/Vs digitized from Figure 3b of Dawson et al. (1999) with contours of resistivity from c) overlaid. Only resolution contours of 0.7 or less are displayed on a) and c), higher values cluster near the surface. See Figure 11 for definition of symbols.

Figure 13. Comparison between the 3D MT inversion and Vp/Vs from Lin et al. (2014a). a) is the resistivity cross-section traverse along the center of a polygon defining the interpreted rift zones

at -1 km elevation from Ryan (1988) with Lin et al. (2014a) Vp/Vs contours overlaid from c). b) is the resistivity along the southwest to northeast traverse with Vp/Vs contours from d) overlaid. c) is the Vp/Vs from Lin et al. (2014a) along the center of a polygon defining the interpreted rift zones at -1 km elevation from Ryan (1988) with resistivity contours from a) overlaid. d) is the Vp/Vs along the southwest to northeast traverse from Lin et al. (2014a) with resistivity contours from b) overlaid. e) is Vp/Vs from Lin et al. (2014a) at elevation -1 km with resistivity contours overlaid. See Figure 11 for definition of symbols.

Figure 14. Calculated melt fraction (θ) from equation (1) for conductive anomalies beneath Kīlauea (pressure 71 MPa – solid lines) and Pu‘u‘ō‘ō (pressure 49 MPa – dashed lines). Workflow follows Zhang et al. (2016). Red curves are for magma water saturation of 0.7 wt% for Kīlauea magmas from Moore et al. (2021).

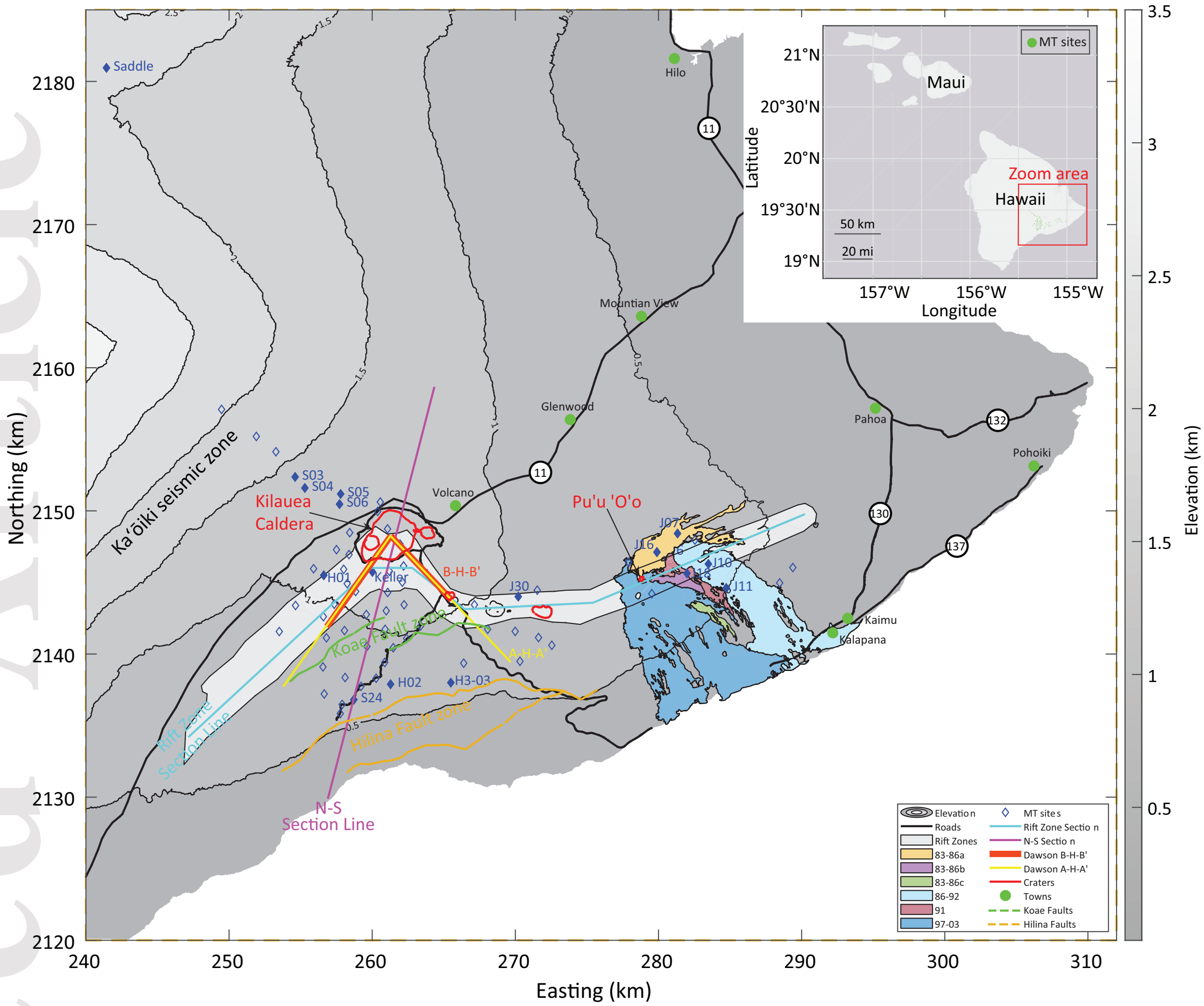

Northing (km)
Easting (km)
Elevation (km)
Saddle
Hilo
Mountian View
Glenwood
Volcano
Pahoa
Pohoiki
Kaimu
Kalapana
Ka'ōiki seismic zone
Kilauea
Caldera
Pu'u 'O'o
S03
S04
S05
S06
H01
Keller
B-H-B'
J30
J07
J16
J10
J11
H02
H3-03
S24
A-H-A'
Koae Fault zone
Hilina Fault zone
Rift Zone
Section Line
N-S
Section Line
11
130
132
137
MT sites
Maui
Hawaii
Zoom area
Latitude
Longitude
21°N
20°30'N
20°N
19°30'N
19°N
157°W
156°W
155°W
50 km
20 mi
Elevation
Roads
Rift Zones
83-86a
83-86b
83-86c
86-92
91
97-03
MT sites
Rift Zone Section
N-S Section
Dawson B-H-B'
Dawson A-H-A'
Craters
Towns
Koae Faults
Hilina Faults

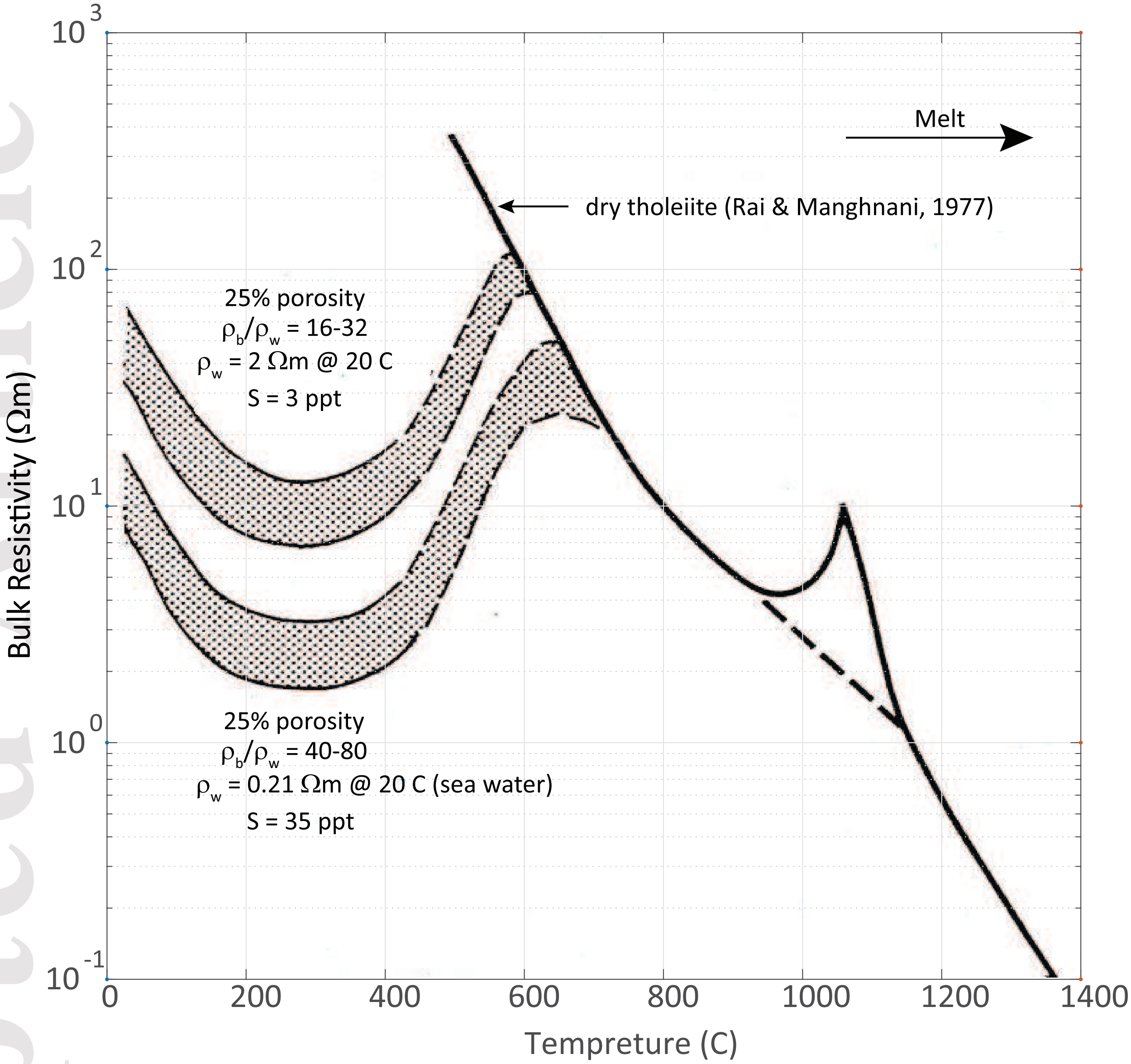

10^3
10^2
10^1
10^0
10^-1
Bulk Resistivity (Ωm)
0
200
400
600
800
1000
1200
1400
Tempreture (C)
Melt
dry tholeiite (Rai & Manghnani, 1977)
25% porosity
ρb/ρw = 16-32
ρw = 2 Ωm @ 20 C
S = 3 ppt
25% porosity
ρb/ρw = 40-80
ρw = 0.21 Ωm @ 20 C (sea water)
S = 35 ppt

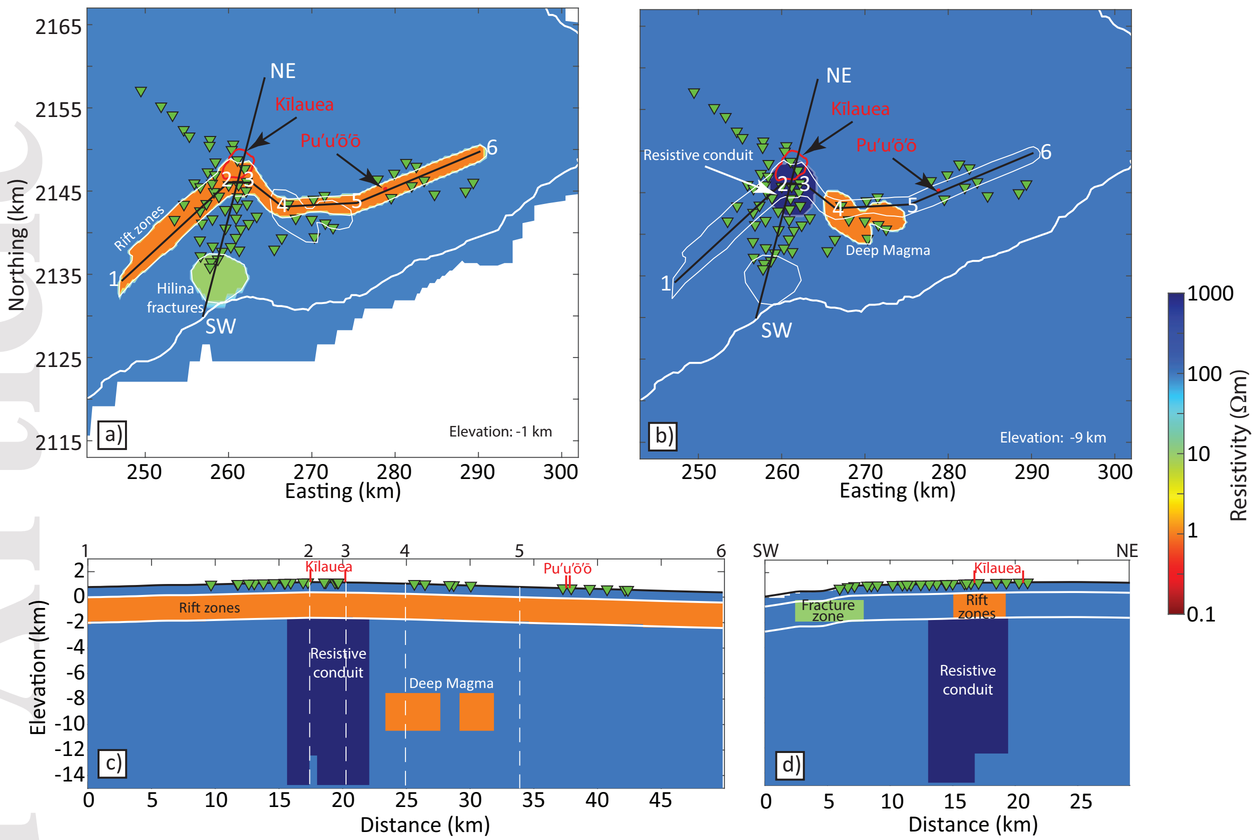

a)
b)
c)
d)
NE
SW
Kīlauea
Pu'u'ō'ō
Rift zones
Hilina fractures
Resistive conduit
Deep Magma
Elevation: -1 km
Elevation: -9 km
Northing (km)
Easting (km)
Elevation (km)
Distance (km)
Fracture zone
Rift zones
Resistivity (Ωm)
1000
100
10
1
0.1

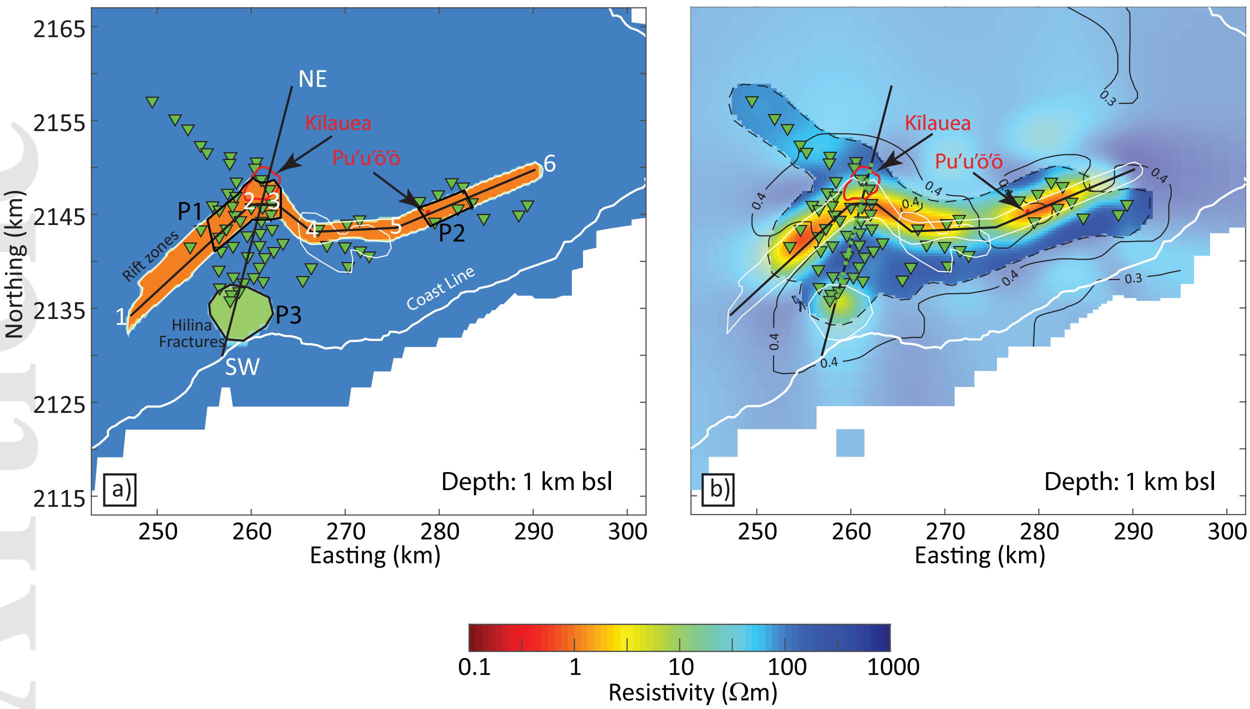

2165
2155
2145
2135
2125
2115
Northing (km)
NE
Kīlauea
Pu'u'ō'ō
P1
P2
P3
Rift zones
Hilina Fractures
SW
Coast Line
a)
Depth: 1 km bsl
250
260
270
280
290
300
Easting (km)
b)
Depth: 1 km bsl
0.1
1
10
100
1000
Resistivity (Ωm)

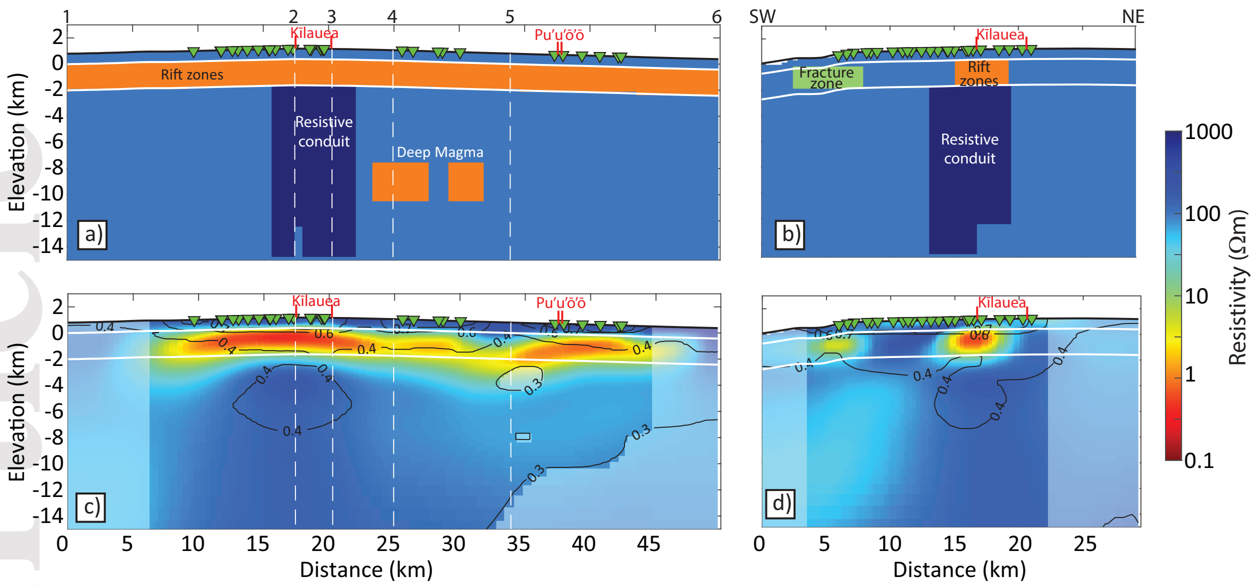

Kīlauea
Pu'u'ō'ō
Rift zones
Resistive conduit
Deep Magma
a)
b)
c)
d)
SW
NE
Fracture zone
Elevation (km)
Distance (km)
Resistivity (Ωm)
1000
100
10
1
0.1

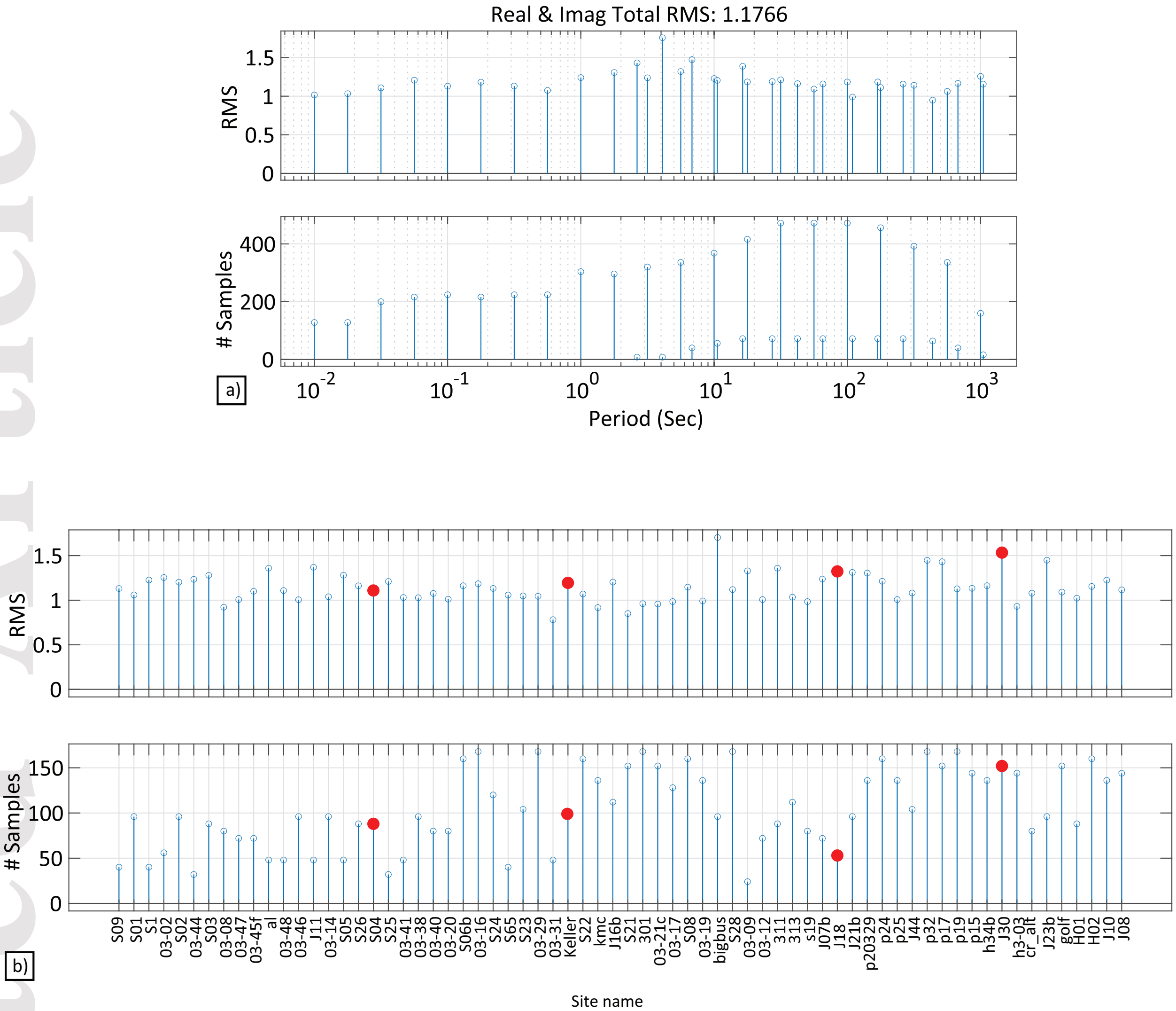

Real & Imag Total RMS: 1.1766
RMS
Samples
a)
Period (Sec)
10^{-2} 10^{-1} 10^{0} 10^{1} 10^{2} 10^{3}
RMS
Samples
b)
Site name
S09 S01 S1 03-02 S02 03-44 S03 03-08 03-47 03-45f al 03-48 03-46 J11 03-14 S05 S26 S04 S25 03-41 03-38 03-40 03-20 S06b 03-16 S24 S65 S23 03-29 03-31 Keller S22 kmc J16b S21 301 03-21c 03-17 S08 03-19 bigbus S28 03-09 03-12 311 313 s19 J07b J18 J21b p20329 p24 p25 J44 p32 p17 p19 p15 h34b J30 h3-03 cr_alt J23b golf H01 H02 J10 J08

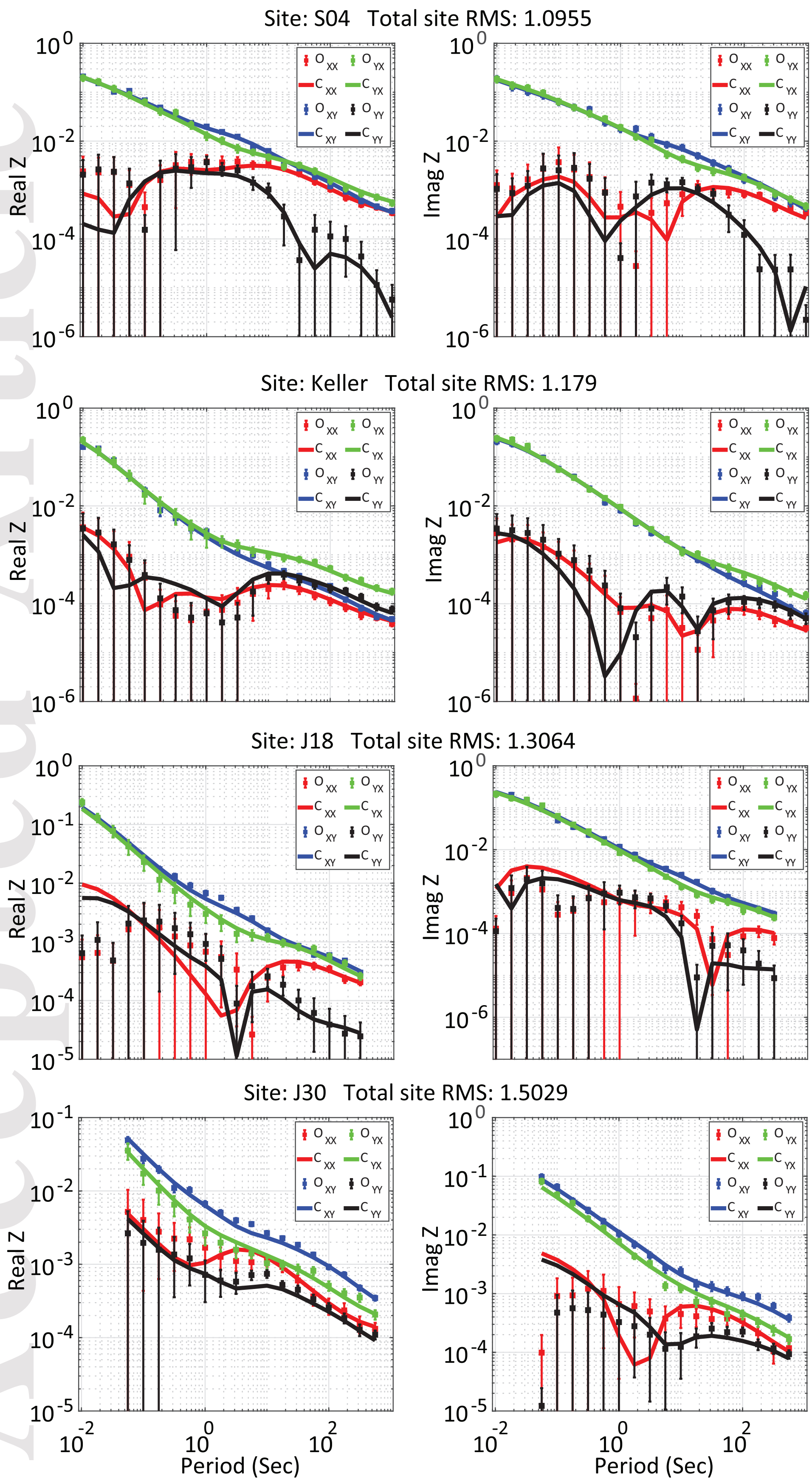
Site: S04 Total site RMS: 1.0955
Site: Keller Total site RMS: 1.179
Site: J18 Total site RMS: 1.3064
Site: J30 Total site RMS: 1.5029
Real Z
Imag Z
O_{XX} O_{YX} C_{XX} C_{YX} O_{XY} O_{YY} C_{XY} C_{YY}
Period (Sec)

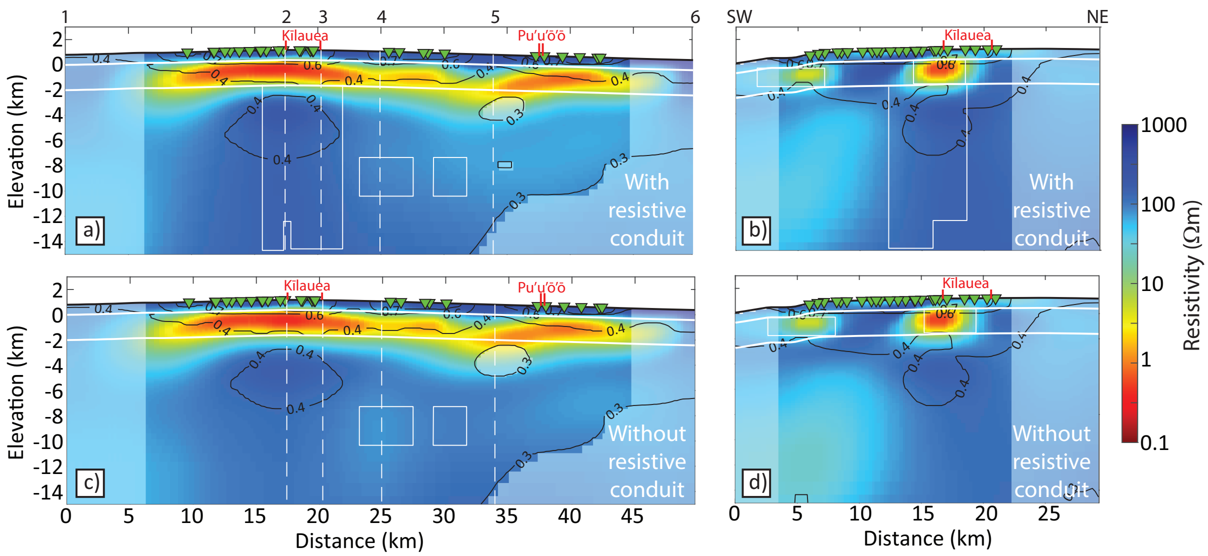

a)
b)
c)
d)
Kīlauea
Pu'u'ō'ō
SW
NE
Elevation (km)
Distance (km)
With resistive conduit
Without resistive conduit
Resistivity (Ωm)

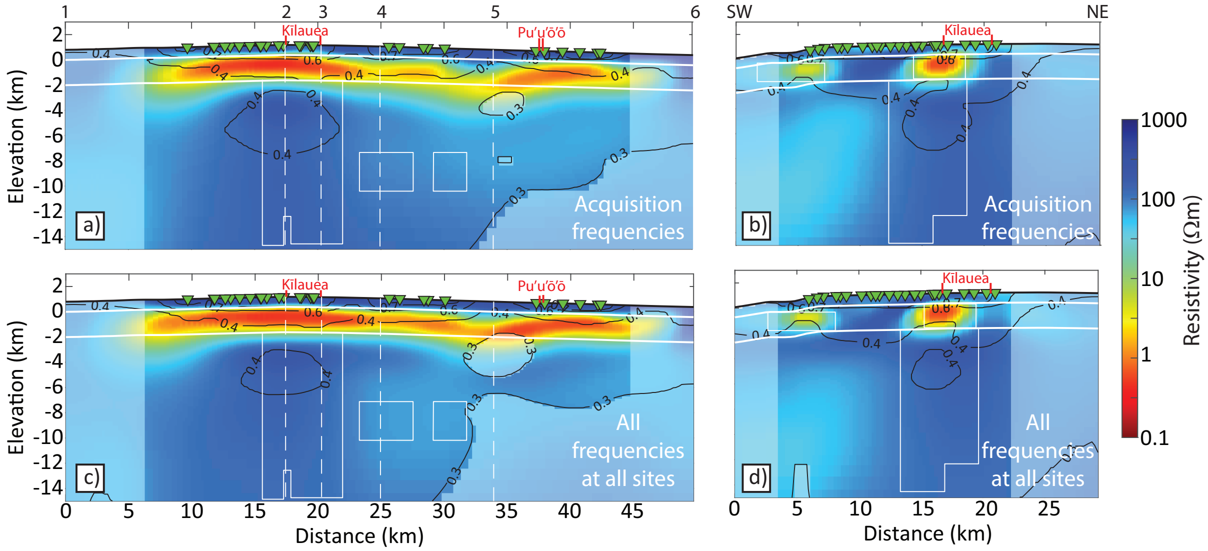

Kilauea
Pu'u'ō'ō
Acquisition frequencies
All frequencies at all sites
a)
b)
c)
d)
SW
NE
Elevation (km)
Distance (km)
Resistivity (Ωm)
1000
100
10
1
0.1

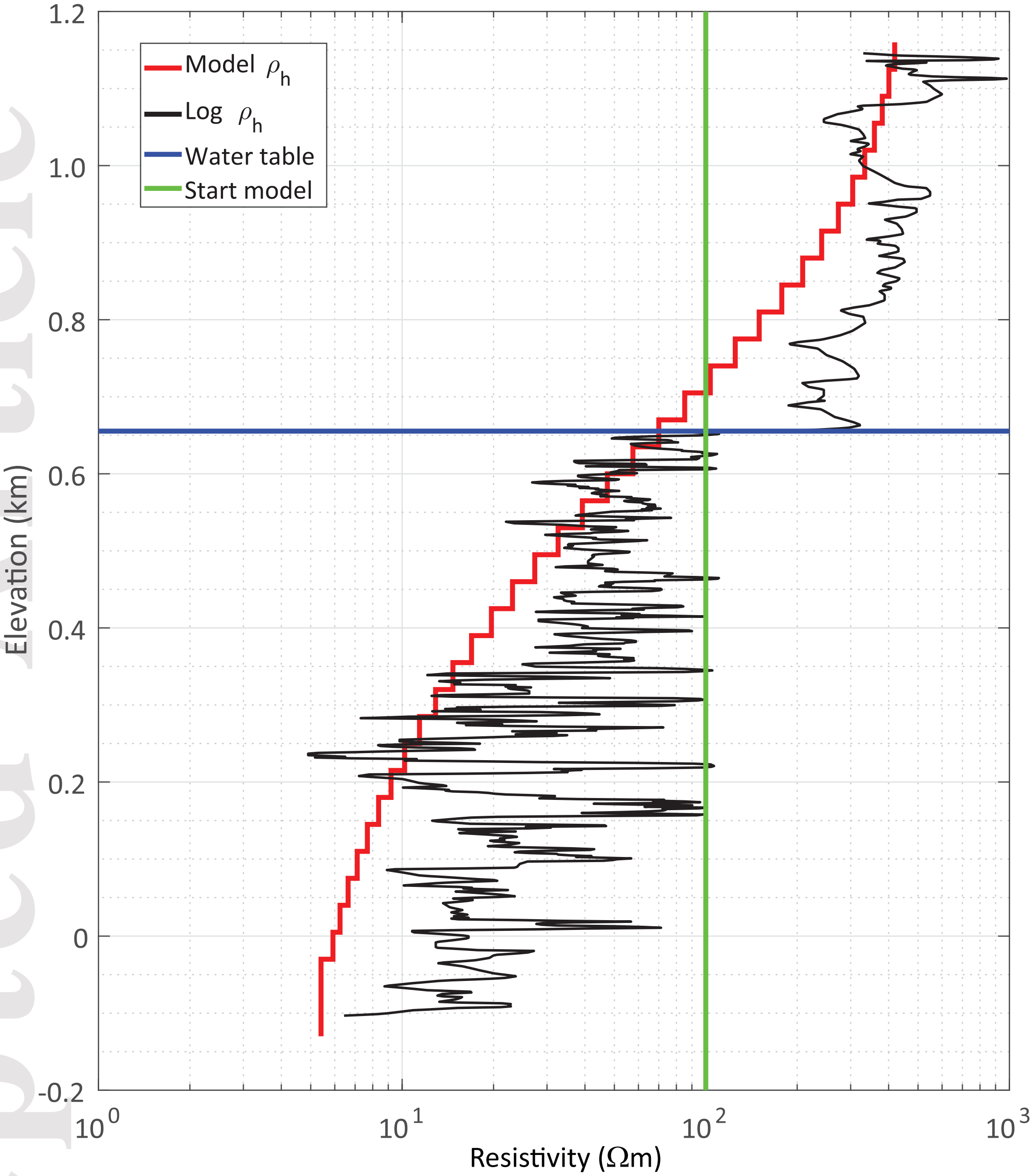

Model ρ_h
Log ρ_h
Water table
Start model
Elevation (km)
1.2
1.0
0.8
0.6
0.4
0.2
0
-0.2
10^0
10^1
10^2
10^3
Resistivity (Ωm)

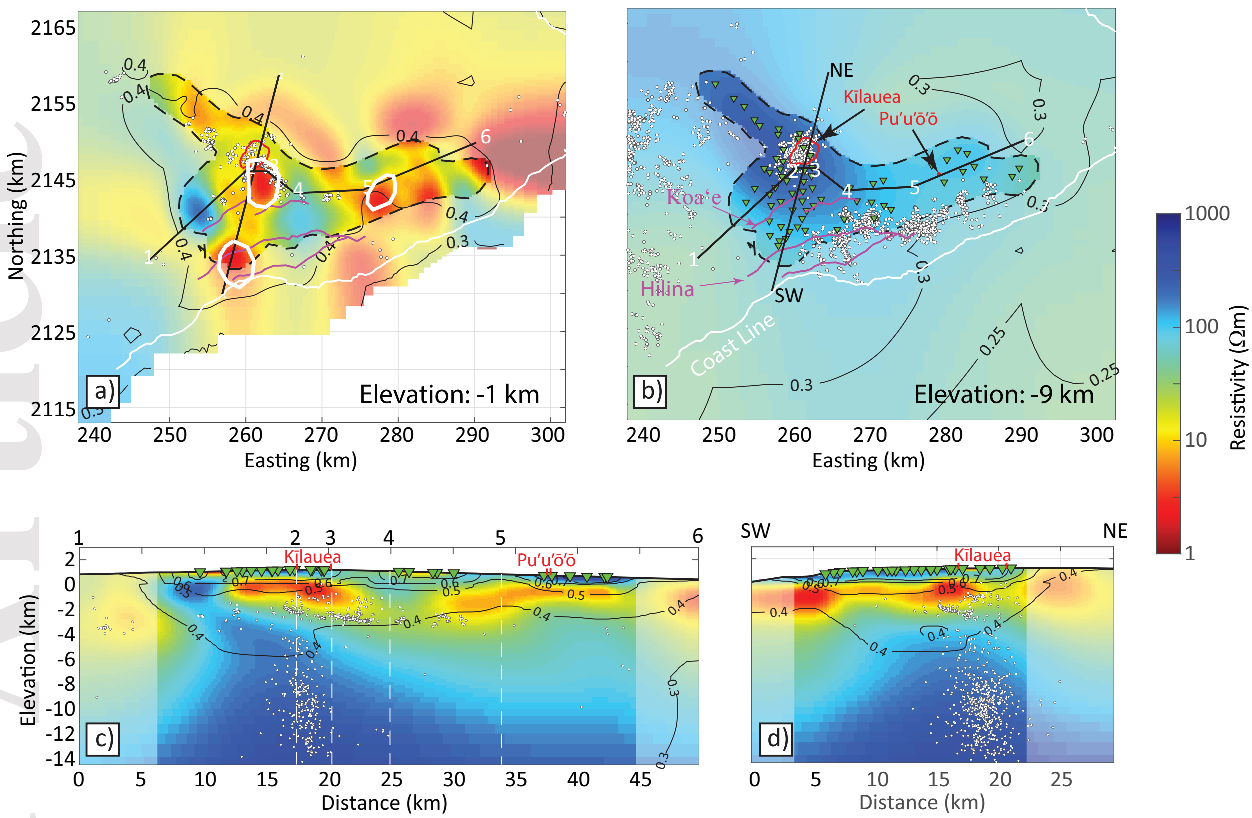

a)
Elevation: -1 km
Northing (km)
Easting (km)
b)
Elevation: -9 km
NE
SW
Kīlauea
Pu'u'ō'ō
Koa'e
Hilina
Coast Line
Easting (km)
Resistivity (Ωm)
1000
100
10
1
c)
Kīlauea
Pu'u'ō'ō
Elevation (km)
Distance (km)
d)
SW
NE
Kīlauea
Distance (km)

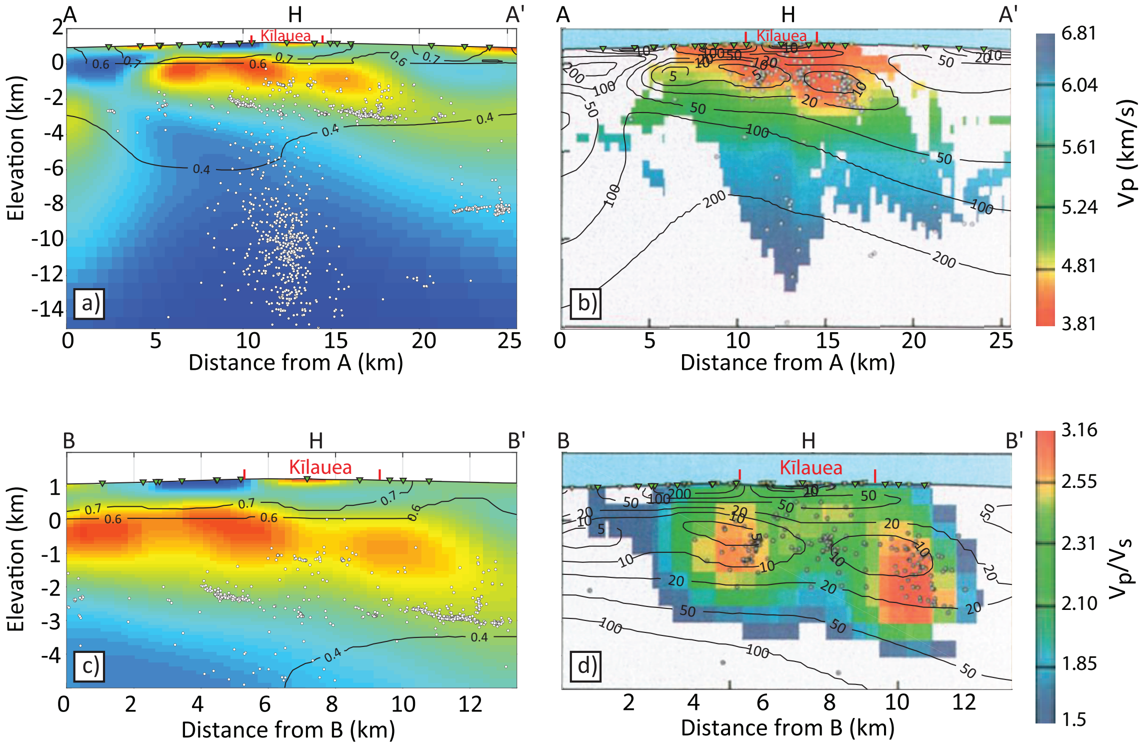

A
H
A'
Kīlauea
Elevation (km)
Distance from A (km)
a)
b)
Resistivity (Ωm)
1000
100
10
1
Vp (km/s)
6.81
6.04
5.61
5.24
4.81
3.81
B
B'
Distance from B (km)
c)
d)
V_p/V_s
3.16
2.55
2.31
2.10
1.85
1.5

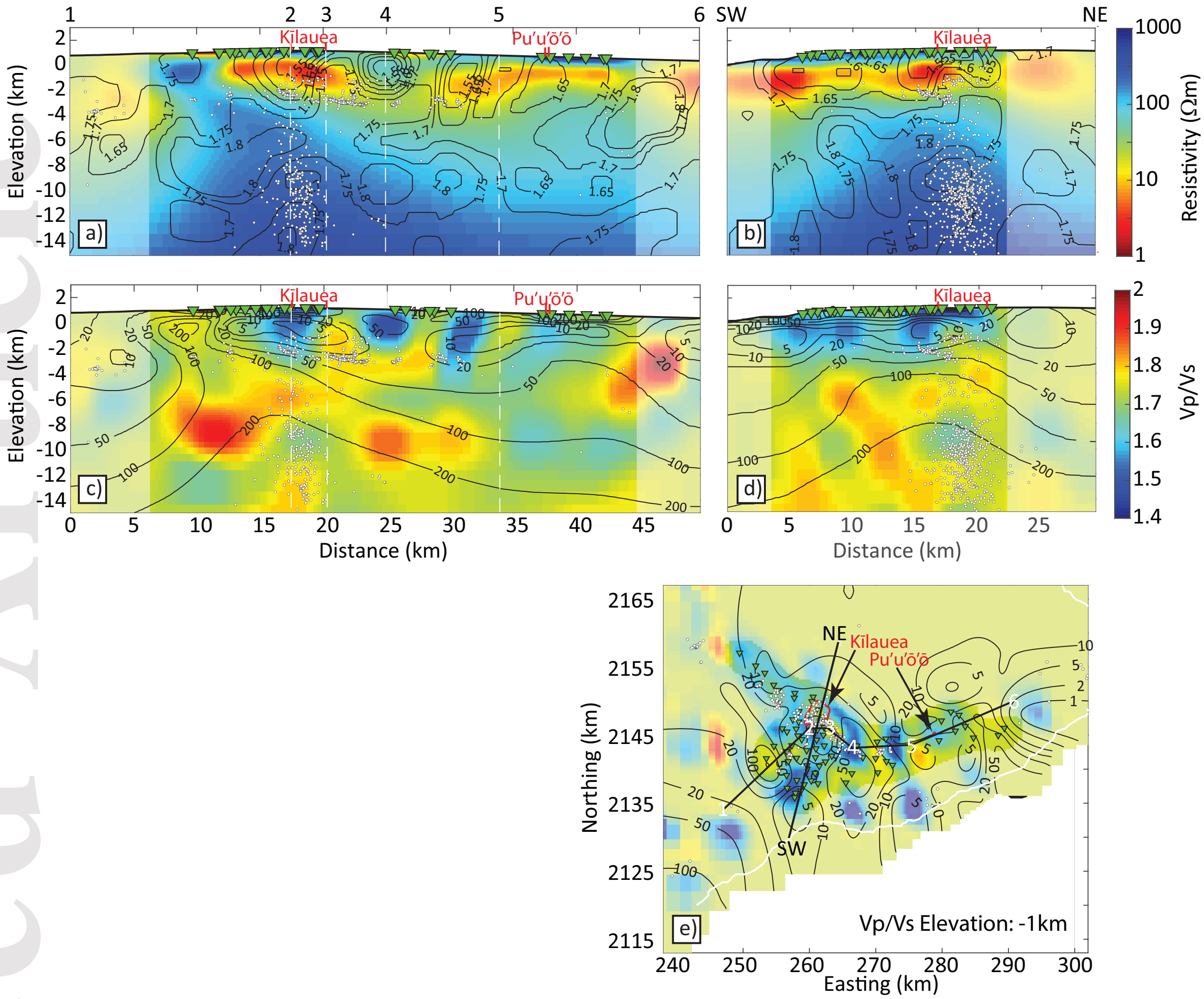

Kīlauea
Pu'u'ō'ō
SW
NE
Elevation (km)
Distance (km)
Resistivity (Ωm)
Vp/Vs
Northing (km)
Easting (km)
Vp/Vs Elevation: -1km
a)
b)
c)
d)
e)

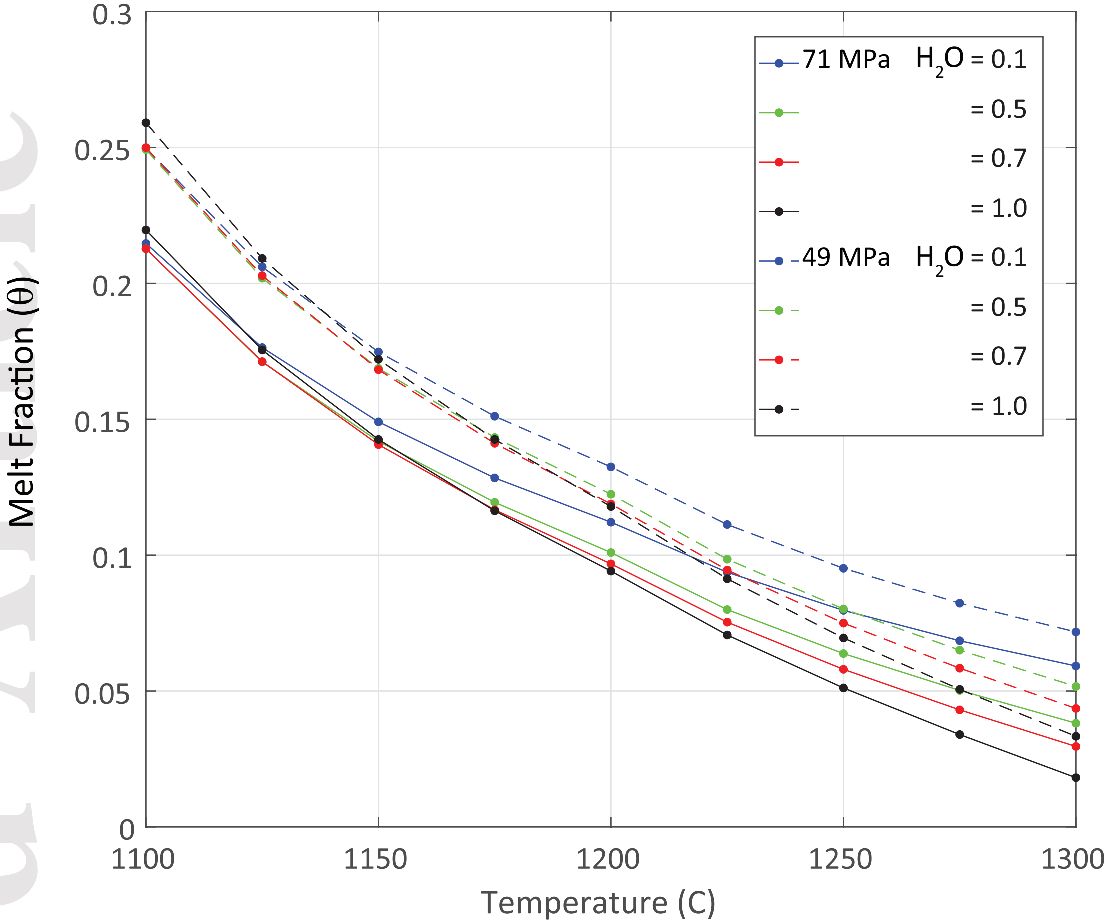

71 MPa H2O = 0.1
= 0.5
= 0.7
= 1.0
49 MPa H2O = 0.1
= 0.5
= 0.7
= 1.0
Melt Fraction (θ)
Temperature (C)
0
0.05
0.1
0.15
0.2
0.25
0.3
1100
1150
1200
1250
1300